



Colloidal Aziridinium Lead Bromide Quantum Dots

Journal Article

Author(s):

Bodnarchuk, Maryna I.; Feld, Leon G.; [Zhu, Chenglian](#) ; Boehme, Simon C.; Bertolotti, Federica; Avaro, Jonathan; Aebli, Marcel; Mir, Showkat Hassan; Masciocchi, Norberto; [Erni, Rolf](#) ; Chakraborty, Sudip; Guagliardi, Antonietta; Rainò, Gabriele; Kovalenko, Maksym V.

Publication date:

2024-02-20

Permanent link:

<https://doi.org/10.3929/ethz-b-000665232>

Rights / license:

[Creative Commons Attribution 4.0 International](#)

Originally published in:

ACS Nano 18(7), <https://doi.org/10.1021/acsnano.3c11579>

Funding acknowledgement:

192308 - Q-Light - Engineered Quantum Light Sources with Nanocrystal Assemblies (SNF)

Colloidal Aziridinium Lead Bromide Quantum Dots

Maryna I. Bodnarchuk,* Leon G. Feld, Chenglian Zhu, Simon C. Boehme, Federica Bertolotti, Jonathan Avaro, Marcel Aebli, Showkat Hassan Mir, Norberto Masciocchi, Rolf Erni, Sudip Chakraborty, Antonietta Guagliardi, Gabriele Rainò, and Maksym V. Kovalenko*



Cite This: *ACS Nano* 2024, 18, 5684–5697



Read Online

ACCESS |

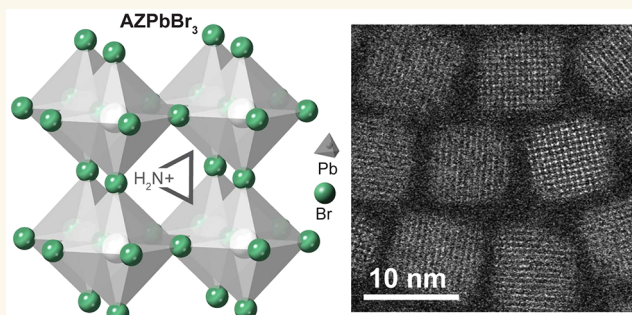
Metrics & More

Article Recommendations

Supporting Information

ABSTRACT: The compositional engineering of lead-halide perovskite nanocrystals (NCs) via the A-site cation represents a lever to fine-tune their structural and electronic properties. However, the presently available chemical space remains minimal since, thus far, only three A-site cations have been reported to favor the formation of stable lead-halide perovskite NCs, i.e., Cs⁺, formamidinium (FA), and methylammonium (MA). Inspired by recent reports on bulk single crystals with aziridinium (AZ) as the A-site cation, we present a facile colloidal synthesis of AZPbBr₃ NCs with a narrow size distribution and size tunability down to 4 nm, producing quantum dots (QDs) in the regime of strong quantum confinement. NMR and Raman spectroscopies confirm the stabilization of the AZ cations in the locally distorted cubic structure. AZPbBr₃ QDs exhibit bright photoluminescence with quantum efficiencies of up to 80%. Stabilized with cationic and zwitterionic capping ligands, single AZPbBr₃ QDs exhibit stable single-photon emission, which is another essential attribute of QDs. In particular, didodecyldimethylammonium bromide and 2-octyldodecyl-phosphoethanolamine ligands afford AZPbBr₃ QDs with high spectral stability at both room and cryogenic temperatures, reduced blinking with a characteristic ON fraction larger than 85%, and high single-photon purity ($g^{(2)}(0) = 0.1$), all comparable to the best-reported values for MAPbBr₃ and FAPbBr₃ QDs of the same size.

KEYWORDS: nanocrystals, quantum dots, aziridinium, perovskite, ligands, photoluminescence



The past decade has seen the discovery and the rapid development of colloidal lead halide perovskite nanocrystals (NCs) of APbX₃ stoichiometry, where A represents the Cs cation or an organic cation, and X indicates a halogen anion.^{1–3} These materials have captured broad interest due to their straightforward synthesis and outstanding optical properties, foremost narrowband photoluminescence (PL) with near-unity quantum yield (QY) and wide spectral tunability (410–750 nm), high absorption coefficients and, at cryogenic temperatures, high radiative rates, and long excitonic coherence times.^{4–7} A rather stringent structural requirement for forming the perovskite lattice (i.e., a three-dimensional (3D) network of corner-shared lead-halide octahedra), usually expressed via the Goldschmidt tolerance factor, is the insertion of A-site cations of an appropriate size. Cs is the only sufficiently large inorganic cation, whereas suitably small and yet chemically robust organic cations include methylammonium (MA) and formamidinium (FA), both extensively used in perovskites as optoelectronic materials. Judicious choices of these three ions in either single-

or mixed-cation compositions enable fine-tuning of electronic properties via, e.g., the octahedral tilt angles, as well as improving materials phase stability and chemical durability in bulk, thin-film, and nanocrystalline forms.^{8–12} Further expanding the thus-far-limited choice for the A-site cation may unlock additional opportunities in the precision engineering of the structural and electronic properties of lead-halide perovskites.

Very recently, the aziridinium cation [(CH₂)₂NH₂⁺, labeled hereafter as AZ], a highly reactive and labile triangular heterocycle, was reported to form stable AZPbX₃ compounds.^{13–15} Seemingly in contradiction to the latter,

Received: November 21, 2023

Revised: January 28, 2024

Accepted: January 31, 2024

Published: February 6, 2024



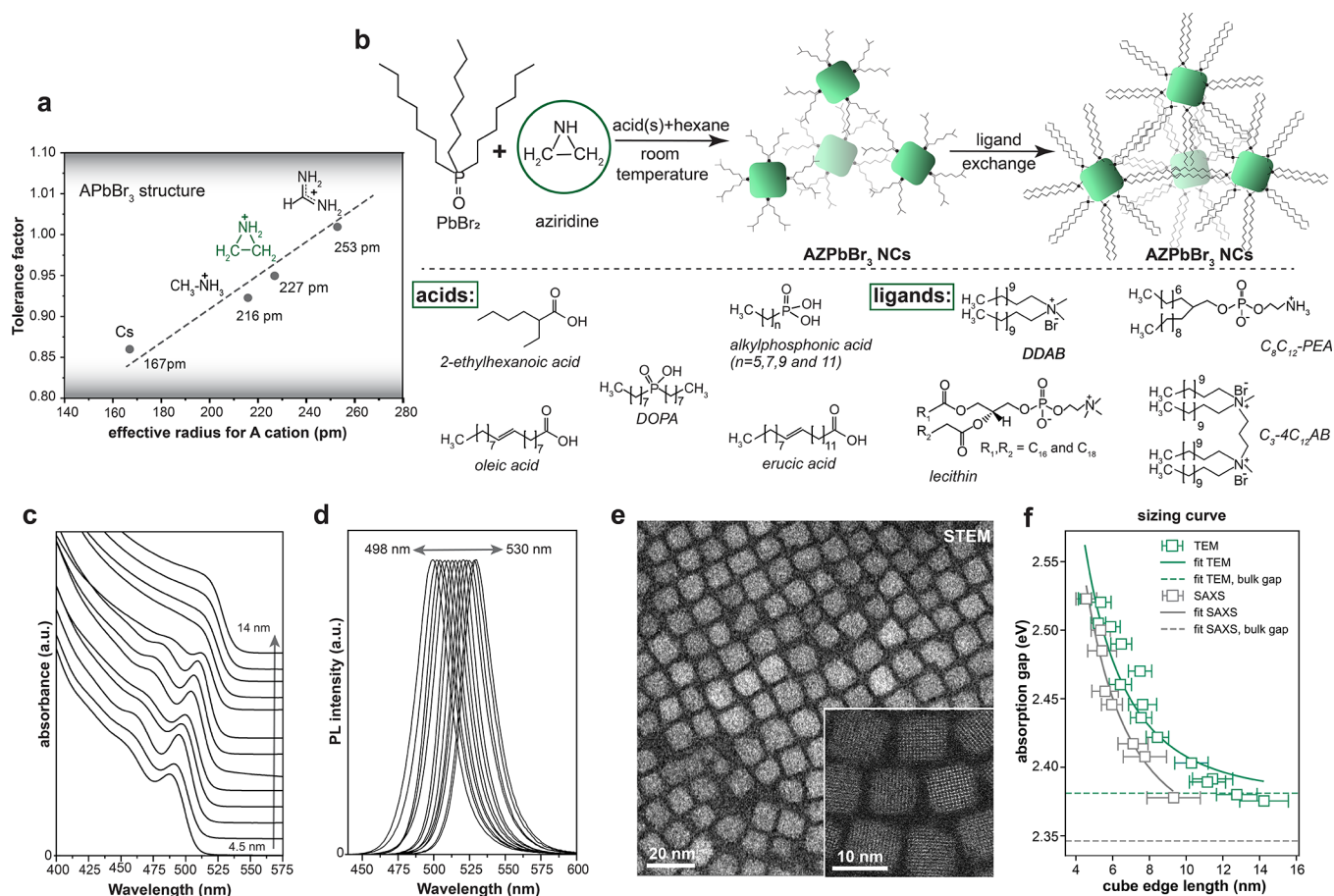


Figure 1. (a) Calculated Goldschmidt tolerance factors for different cations (cesium, methylammonium, aziridinium, and formamidinium) in the APbBr₃ perovskite lattice. (b) Top panel: a reaction scheme; bottom panel: an overview of carboxylic and phosphonic acids as well as ligands used in the synthesis. (c) Optical absorption and (d) PL spectra of purified AZPbBr₃ NCs ranging from 4.5 to 14 nm in size (for visualization purposes, a cumulative vertical offset was applied to each subsequent spectra). (e) A high-angle annular dark field-scanning transmission electron microscopy (HAADF-STEM) image of purified 8 nm NCs with a high-resolution HAADF-STEM image of few single NC in the inset. (f) Size-dependent (absorption) band gap in AZPbBr₃ NCs for sizes obtained via TEM (green) and SAXS (gray); the experimental data sets (open squares, with error bars denoting the standard deviation) were fitted by a semiempirical sizing curve (solid line), with the bulk band gap (dashed lines) as one of the fit parameters.

computational assessments of the ring opening within the formed perovskite A-site voids had yielded an enthalpy difference of 0.7 eV per formula unit (f.u.) in favor of ring opening in AZPbI₃.¹⁶ However, this value is smaller than the computed and experimental ring-strain energies of ca. 27 kcal/mol (1.16 eV/f.u.),^{17,18} suggesting an overall stabilizing effect by the Pb-halide cage as a “counter-strain” due to the A-site being too small for the opened ring. Furthermore, several favorable formation conditions exist. First, the size of the three-membered AZ ring cation is similar to that of the commonly used MA cation, and the Goldschmidt tolerance factor for AZPbBr₃ is 0.95 (the used ionic radii are $r_{\text{Br}} = 196$ pm, $r_{\text{Pb}} = 119$ pm, $r_{\text{AZ}} = 227$ pm),¹⁹ well within the perovskite formability limits (Figure 1a). Second, the thermodynamic stability of AZPbX₃ (as well as that of Sn analogues) has been anticipated in first-principles calculations focused on the ionization energy of the A-site as a stability predictor.^{19–22} Since the AZ moiety, in its neutral form, exhibits a lower ionization energy than (neutral) MA, with a value closely resembling that of atomic Cs, AZPbX₃ phases were expected to be more stable than MAPbX₃ with thermochemical calculations further supporting the formation of stable perovskite phases. A remaining concern is the reactivity of AZ

(polymerization, nucleophilic attack on the ring, etc.), which also breaks its cyclic nature. However, here again, the perovskite cage apparently guards the AZ cations, as seen from the air stability of the reported AZPbX₃ compounds.^{13–15} Additionally, strong steric requirements provided by the size and shape of the “reaction cavity” within the crystal lattice may increase the actual activation energy for any thermodynamically allowed transformation to a threshold not easily achievable if no additional power is provided (in the form of heat or light). Indeed, when the space surrounding the molecules becomes restricted, their reactivity and related behavior can be significantly altered.²³

In this work, we explored the prospects of AZ-based perovskite NCs as a potentially powerful addition to the family of highly luminescent MA/FA/Cs lead halide NCs. We focused on the AZPbBr₃ composition and devised the synthesis of monodisperse and size-tunable NCs in strong and weak quantum-confinement regimes, e.g., QDs. The preparation of AZPbBr₃ NCs leveraged the recently reported room-temperature synthesis platform based on PbBr₂/trioctylphosphine oxide (TOPO) molecular adducts as the precursor,²⁴ wherein the formation of NCs is precisely adjustable and traceable in situ, due to slower reaction

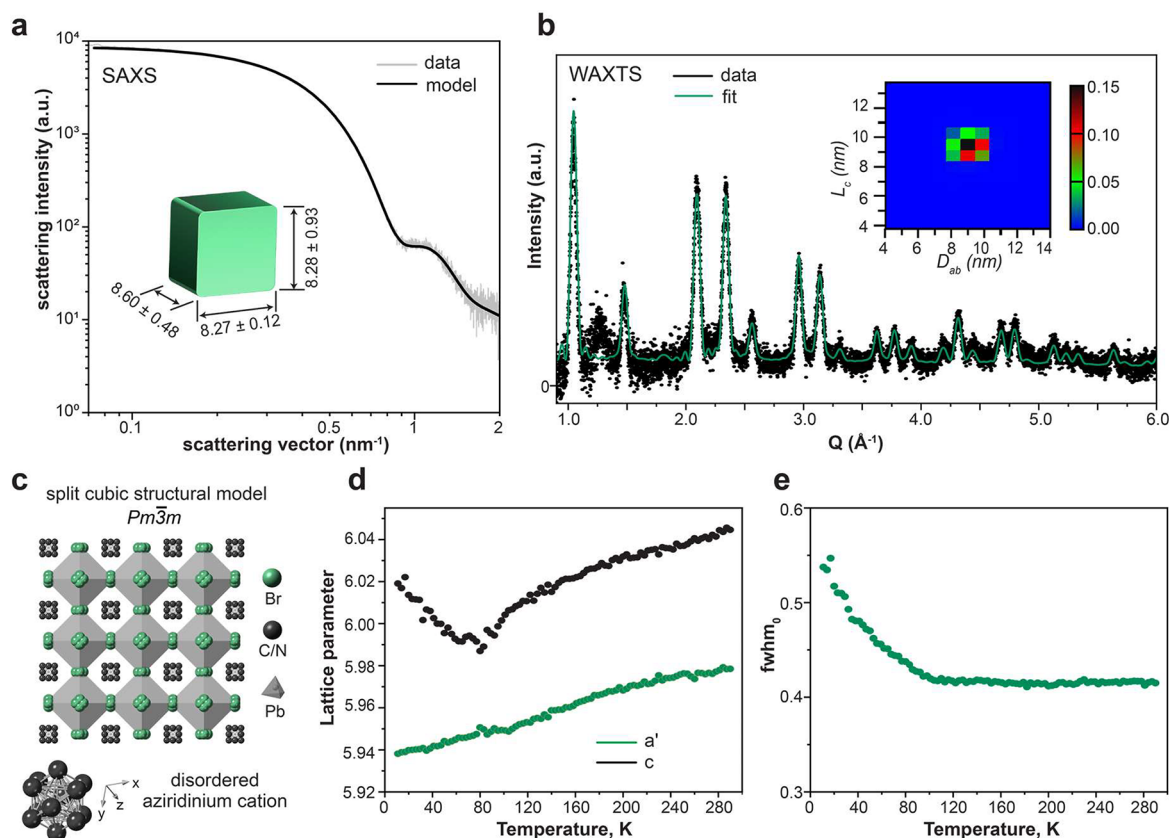


Figure 2. (a) The fit of experimental SAXS data from an AZPbBr₃ NC colloidal suspension (gray line) via an analytical model (black line) yields cuboids with edge lengths of 8.27 ± 0.12 , 8.28 ± 0.93 , and 8.60 ± 0.48 nm, respectively. (b) Solvent-subtracted synchrotron WAXTS data (black line) and the best fit (green line) of AZPbBr₃ NCs using the split cubic model with locally tilted/disordered PbBr₆ octahedra (for a more extended discussion, see the [Supporting Information](#)); the inset shows a 2D map of the refined (number-based) log-normal size distribution function (D_{ab} : the diameter of the circle of area equivalent to the prisms basal plane and L_c , the height of the prismatic clusters). (c) The split cubic structural model of AZPbBr₃ NCs (the four Br of each PbBr₆ octahedra, shown in green, have 1/4 site occupancy factor each, i.e., only one out of four is stochastically present in each site) and the model of AZ cation formed by disordering in 12 symmetry-equivalent orientations (4 equivalent geometrical orientations \times 3 “elemental” C–C/N dispositions, H atoms were omitted, similar to bulk AZPbBr₃). (d) The temperature dependence of the tetragonal unit cell parameters $a' = a/\sqrt{2}$ and c for a weakly distorted (ca. 1%) cubic lattice, plotted in the entire 11–290 K range, showing an anomaly below 90 K. (e) The temperature dependence of the fwhm_0 parameter (the θ -dependence of the peak width is described according to the relation $\text{fwhm}(\theta) = \text{fwhm}_0/\cos \theta$), which suggests additional peak broadening (hidden splitting) below 90 K.

kinetics, compared to more traditional hot-injection or solvent-assisted reprecipitation methods. Furthermore, this PbBr₂/TOPO synthesis benefits from the decoupling of the NC formation and subsequent coating with the capping ligand of choice before the purification and isolation of NCs. We tested several state-of-the-art capping ligands, cationic and zwitterionic, and found that didodecyldimethylammonium bromide (DDAB) and 2-octyldodecyl-phosphoethanolamine (C₈C₁₂-PEA) ligands render AZPbBr₃ NCs robust for both ensemble and single-particle studies. Their photostability, high ON-fraction (>85%) in blinking studies, and high single-photon purity ($g^{(2)}(0)$ as low as 0.1) render AZPbBr₃ NCs comparable to the best reported MAPbBr₃ and FAPbBr₃ NCs.²⁵

RESULTS AND DISCUSSION

Synthesis of AZPbBr₃ NCs. The room-temperature synthesis of AZPbBr₃ QDs proceeds through rapid injection of an aziridine solution in chloroform or dibromomethane (see further details in [Figure 1b](#) and the [Supporting Information](#)) into a precursor solution comprising PbBr₂/TOPO adduct, diisooctylphosphinic (DOPA), and alk(en)ylcarboxylic acids

(2-ethylhexanoic acid, oleic acid, or erucic acid) in hexane, with the optional addition of alkylphosphonic acids (for obtaining the smallest NCs; see the subsequent discussion). We note that AZ cations cannot be formed ex situ for use as a stable precursor, due to their high ring instability in common solvents. Instead, AZ cations form in situ, because of the high acidity of the PbBr₂/TOPO precursor solution (aziridine:DO-PA:carboxylic acids molar ratios = 1:8.5:17). TOPO, DOPA, and alkyl carboxylic acids are known as weakly binding ligands for perovskite NCs.²⁴ They can be readily displaced by more strongly binding alternatives such as didodecyldimethylammonium bromide (DDAB),^{26,27} custom-engineered zwitterionic phospholipid ligand [2-octyldodecylphosphoethanolamine (C₈C₁₂-PEA)],²⁵ or the commercially available natural phospholipid lecithin,²⁸ followed by purification and isolation steps. This procedure yields stable colloids of highly monodispersed cuboidal AZPbBr₃ NCs exhibiting bright green emission and high stability over long-term storage in air ([Figure S1](#)).

The size of NCs was adjusted between 4.5 and 14 nm in diameter, resulting in tunable absorption and PL, with PL peaks in the range from 498 to 530 nm (see [Figures 1c](#) and [1d](#),

as well as Figures S2 and S3 and Table S1), by manipulating the reaction time (the time delay between the injection of the aziridine solution and the injection of the ligand solution was typically 10–240 s) as well as by introducing various amounts of alkylphosphonic acids (hexyl-, octyl-, decyl-, or dodecylphosphonic acid) into the $\text{PbBr}_2/\text{TOPO}$ precursor solution. Phosphonic acids slow the reaction kinetics, facilitating the preparation of strongly confined AZPbBr_3 NCs (down to 4.5 nm, Figure S2d). Conversely, utilizing mesitylene as a reaction solvent and a longer reaction time yields NCs larger than 10 nm, with PL peaks from 525 to 530 nm. The overall dilution of precursors does not significantly alter the PL peak of AZPbBr_3 (Figure S2c), unlike in the synthesis of CsPbBr_3 NCs.²⁴ Importantly, a narrow size dispersion of AZPbBr_3 NCs can be reached only under a high Pb-precursor excess (aziridine:Pb molar ratio = 1:4). The minute-scale formation kinetics of AZPbBr_3 NCs allow in situ optical monitoring with ultraviolet-visible light (UV-vis) absorption, as exemplified for 6.5 nm samples (Figure S4).

DDAB-capped AZPbBr_3 NCs are sharp cuboids, in agreement with the known tendency of cationic ligands to stabilize the set of (100) facets.^{26,29,30} C_8C_{12} -PEA-coated NCs are rather truncated, presumably due to surface reconstruction or etching (see Figure S3 and Table S1). Lower colloidal robustness was observed when employing the recently reported dicationic ligands (propanediyl-1,3-*N,N*-bis-(didodecylmethylammonium bromide), $\text{C}_3\text{-4C}_{12}\text{AB}$)³¹ or lecithin. The AZPbBr_3 NCs capped with DDAB or C_8C_{12} -PEA exhibit an average PL QY of $80\% \pm 2\%$ for NC sizes between 8 and 10 nm, and the PL QY increases up to $90\% \pm 4\%$ for samples prepared with the addition of phosphonic acids (4.5–8 nm).

Electron Microscopy and SAXS Studies. The high-angle annular dark field-STEM (HAADF-STEM) and high-resolution HAADF-STEM images evidence the (100) termination of the DDAB-capped NC surfaces (Figure 1e; synthesis without phosphonic acids, 20 s reaction labeled as “standard” in Table S1). Shape retrieval from small-angle X-ray scattering (SAXS, Figure 2a) yields a slightly prolate cuboid shape (aspect ratio of ca. 1.04) with the lengths of the three NC edges being 8.27 ± 0.12 , 8.28 ± 0.93 , and 8.60 ± 0.48 nm (that is, substantially isotropic; see Figure S5 and Table S2 in the Supporting Information for SAXS data of an extended NC size series).

Sizing Curve. Figure 1f presents the size dependence of the band gap energies in AZPbBr_3 , using the NC size determined via either TEM or SAXS, and the band gap estimated from the lowest-energy minimum of the second derivative of the absorbance (see the Supporting Information for details). Such a “sizing curve” is of great practical utility as an express method for obtaining the approximate NC size using only a standard UV-vis spectrometer. Furthermore, the size dependence associates with the basic electronic structure of the underlying bulk material. Within the semiempirical expression derived in Aubert et al.,³² (see the Supporting Information for the equation and further details), the functional form of the size dependence for a wide range of semiconductors is given by only three bulk parameters: the bulk band gap (E_0), the reduced mass (μ) of the exciton, and the dielectric constant (ϵ_∞) at the optical frequency (see the Supporting Information for further details). In Figure 1f, we have tested the inverse of this idea by fitting our experimental AZPbBr_3 size-dependent band gap (open squares) with the semiempirical expression

(solid line) given by Aubert et al.,³² hereby yielding approximate estimates for the thus far still ill-defined electronic parameters for bulk AZPbBr_3 . To limit the parameter space and stabilize the fit, we keep the bulk band gap E_0 and the reduced mass μ as free fit parameters and estimate the dielectric constant ϵ_∞ with the help of DFT calculations (see Table S5 and associated details in the Supporting Information). For the SAXS dataset, the best fit is obtained for the following parameters: $E_0 = 2.35$ eV (fitted), $\mu = 0.17$ (fitted), and $\epsilon_\infty = 8.25$ (fixed; based on our DFT calculations 13% higher than for CsPbBr_3 ³³), translating into a Bohr diameter d_0 of about 5.0 nm. Similar fit parameters are also obtained for the TEM dataset, albeit with a slightly higher estimate for the bulk band gap. Overall, we conclude that the electron and hole effective masses, dielectric constant, and, thus, the exciton Bohr diameter should be comparable in AZPbBr_3 and CsPbBr_3 (see also Tables S4–S6),^{32,34} while the bulk band gap of AZPbBr_3 appears few tens of millielectronvolts lower than in CsPbBr_3 ($E_0 = 2.38$ eV in CsPbBr_3).³⁵ We also note that a previous estimate for the bulk AZPbBr_3 band gap by Petrosova et al.¹³ found an even lower value (2.27 eV); however, their different definition for the band gap (via the zero-crossing in a Tauc plot) precludes a direct comparison to the values found by us for AZPbBr_3 and by Mannino et al.³⁵ for CsPbBr_3 (in both cases defined via second derivatives).

Crystal Structure. The crystal structure of AZPbBr_3 NCs suspended in cycloheptane was investigated with synchrotron X-ray total scattering methods. Bulk AZPbBr_3 was previously reported to crystallize in the cubic lattice with a $Pm\bar{3}m$ space group symmetry and ordered Br atoms with a straight Pb–Br–Pb bond angle of 180° .¹³ However, evidence of local and dynamic symmetry breaking has been found in various lead-halide perovskites that exhibit a long-range cubic structure.^{36–40} We account for local symmetry breaking with a split-cubic perovskite model, for a disordered AZ cation with a cuboctahedral cluster, and for disorder of Br anions into four equivalent positions, as well as a cuboidal NC morphology with the Debye scattering equation. The resulting fit to the wide-angle X-ray total scattering (WAXTS) data is shown in Figure 2b, together with a 2D map of the refined bivariate log-normal size-distribution function. Figure 2c displays the obtained structure, with Pb–Br–Pb bond angles deviating by 13° from the 180° angle expected for an ideal cubic structure. Deviations of similar magnitude are also found in FAPbBr_3 , FAPbI_3 , and FASnI_3 NCs,^{8,12,41–43} corroborating that AZPbBr_3 NCs share the locally broken crystal symmetry. Furthermore, AZPbBr_3 NCs exhibit a slight lattice expansion of $\sim 0.10\%–0.15\%$ with respect to the bulk value, similar to many other nanosized samples of lead-halide perovskites (Table S3).^{44–46} We further uncover signs of a noncubic long-range structure. A small deviation in lattice parameters from a cubic cell (with the c axis about 1% larger than the $a = b$ axis) suggests that the average cell is tetragonal (see Figure S6 and the pertinent discussion in the Supporting Information).

To further understand the crystal symmetry, we performed variable-temperature WAXTS measurements of dried NCs loaded into a glass capillary and collected 93 WAXTS scattering patterns (at 3 K steps, from 11 K to room temperature; see the Supporting Information). Similar to the RT WAXTS data of the solution-phase NCs, also the RT crystal metrics of the dried NCs suggest a distortion from the cubic lattice when analyzed according to the structureless Le Bail method (which avoids the occurrence of the nonrandom

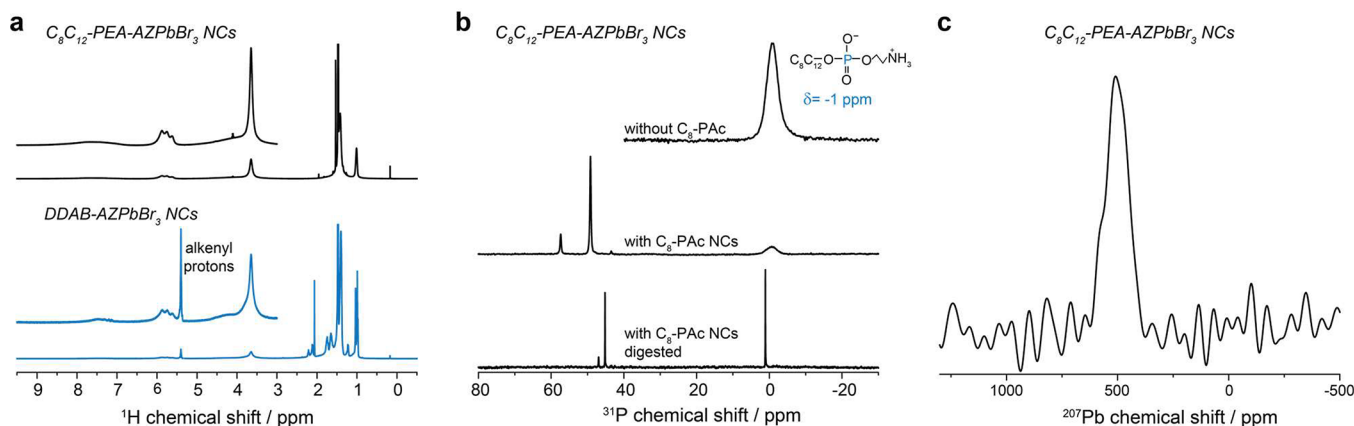


Figure 3. (a) Solution ^1H NMR spectra of C_8C_{12} -PEA (black line) and DDAB-capped (blue line) AZPbBr_3 NCs in cyclohexane- d_{12} . (b) Solution ^{31}P NMR spectra of C_8C_{12} -PEA-capped AZPbBr_3 NCs synthesized without (top) and with (middle) addition of alkylphosphonic acid (for instance, octylphosphonic acid- C_8PAC) during the synthesis and after their further digestion with $\text{DMSO-}d_6$ (bottom). (c) Solid-state ^{207}Pb NMR spectrum of C_8C_{12} -PEA-capped AZPbBr_3 NCs.

orientation distribution function of the NCs and is fully unbiased by errors in the structural model). With decreasing temperature, the crystal unit cell volume monotonously decreases. More importantly, an additional symmetry change is found below 90 K (Figure 2d). From 90 to 11 K, the peak widths progressively increase (Figure 2e), suggesting an additional peak splitting (partially hidden under the broad Bragg peaks), which is consistent with a symmetry-lowering transition to an orthorhombic metric, as observed also in other 3D lead-halide perovskites.

Computational Study. Having elucidated the experimentally observed crystal structure of the synthesized AZPbBr_3 NCs, we further consider the crystal stability via a computational approach. The Goldschmidt tolerance factor (t)⁴⁷ is used extensively to predict the formation and stability of the perovskite structure. However, some studies suggested that a revision of the Goldschmidt tolerance factors may be required.⁴⁸ Recently, Bartel et al. introduced a different tolerance factor⁴⁹

$$\tau = \frac{r_{\text{Br}}}{r_{\text{Pb}}} - n_{\text{AZ}} \left(n_{\text{AZ}} - \frac{r_{\text{AZ}}}{r_{\text{Pb}}} \frac{1}{\ln(r_{\text{AZ}}/r_{\text{Pb}})} \right) \quad (1)$$

with n_{AZ} representing the oxidation state of the AZ-cation and a value of $\tau < 4.18$ suggests a perovskite structure. We estimated $\tau = 3.30$ for AZPbBr_3 , further supporting the perovskite structure formation (the ionic radii used in the present work were $r_{\text{Br}} = 196$ pm, $r_{\text{Pb}} = 119$ pm, $r_{\text{AZ}} = 227$ pm, and $n_{\text{AZ}} = 1$).

To investigate the stability of AZPbBr_3 , we considered the formation reaction equation $(\text{CH}_2)_2\text{NH}_2\text{Br} + \text{PbBr}_2 \rightarrow (\text{CH}_2)_2\text{NH}_2\text{PbBr}_3$ and the corresponding reaction enthalpy:¹⁹

$$\Delta H_r = E_{\text{tot}}[(\text{CH}_2)_2\text{NH}_2\text{PbBr}_3] - E_{\text{tot}}[(\text{CH}_2)_2\text{NH}_2\text{Br}] - E_{\text{tot}}[\text{PbBr}_2] \quad (2)$$

A negative reaction enthalpy would indicate a stable perovskite structure. To obtain the total energy (E_{tot}) of the reactant and products, we performed density functional theory (DFT) calculations, employing the PBE exchange-correlation functional with van der Waals (vdW) corrections. We further considered an orthorhombic AZPbBr_3 crystal structure, the most stable phase at 0 K calculations, in coarse agreement with the lower-than-tetragonal symmetry in our low-temperature X-ray total scattering data (see Supporting Information for

further details, including a discussion of the likelihood of polymorphism). We then obtained negative ΔH_r values of -0.362 eV and -0.373 eV with and without spin-orbit coupling, respectively, affirming the stability of AZPbBr_3 . The respective electronic-structure calculations show a direct band gap of AZPbBr_3 . The conduction band originates from Pb p orbitals, while the valence band is predominantly of Br p character, consistent with other lead halide perovskites (see the Supporting Information for details (Figures S7 and S8, and Tables S7 and S8).

NMR Study. The ligand chemistry of C_8C_{12} -PEA and DDAB-capped AZPbBr_3 NCs was elucidated with NMR experiments performed in solution and the solid state. ^1H solution NMR spectra for both C_8C_{12} -PEA and DDAB-capped AZPbBr_3 NCs confirm the presence of the corresponding capping ligand (Figure 3a). DDAB-capped NCs do not sustain more than one washing cycle, after which a free alkyl carboxylic acid (in this case, oleic acid) is still detected in the DDAB-sample (as alkenyl protons at 5.4 ppm). We thus inspected the C_8C_{12} -PEA-capped NCs in greater detail, since they can be purified at least three times without a notable loss of NC dispersibility. Already twice-washed samples lack any oleate-related signal. ^{31}P NMR spectra evidence the surface-bound C_8C_{12} -PEA ligands in solution (Figure 3b) and in the solid state (Figure S10b). The twice-washed C_8C_{12} -PEA- AZPbBr_3 sample shows only a broad signal centered at approximately -1 ppm from bound C_8C_{12} -PEA (Figure 3b, top). No other signals were detected, excluding free or surface-bound TOPO and DOPA. We also analyzed the NCs synthesized with the addition of alkyl phosphonic acids (Figure 3b, middle), whose ^{31}P NMR signal is expected at 25–28 ppm (see the octylphosphonic acid spectrum in Figure S9 and ref 50). Colloids washed only once exhibit a broad surface-bound C_8C_{12} -PEA signal at -1 ppm and three narrow peaks in the range of 40–60 ppm (absent in twice-washed NC samples), originating from the residual TOPO (49 ppm) and DOPA (57 and 43 ppm for its main impurity). These NC cores were then digested by the addition of $\text{DMSO-}d_6$, liberating surface-bound species, leading to a narrow signal from the free C_8C_{12} -PEA ligand (Figure 3b, bottom) and solvent-related shifts from the TOPO/DOPA species but still no signatures of phosphonic acids. We thus conclude that the small quantities of alkylphosphonic acids

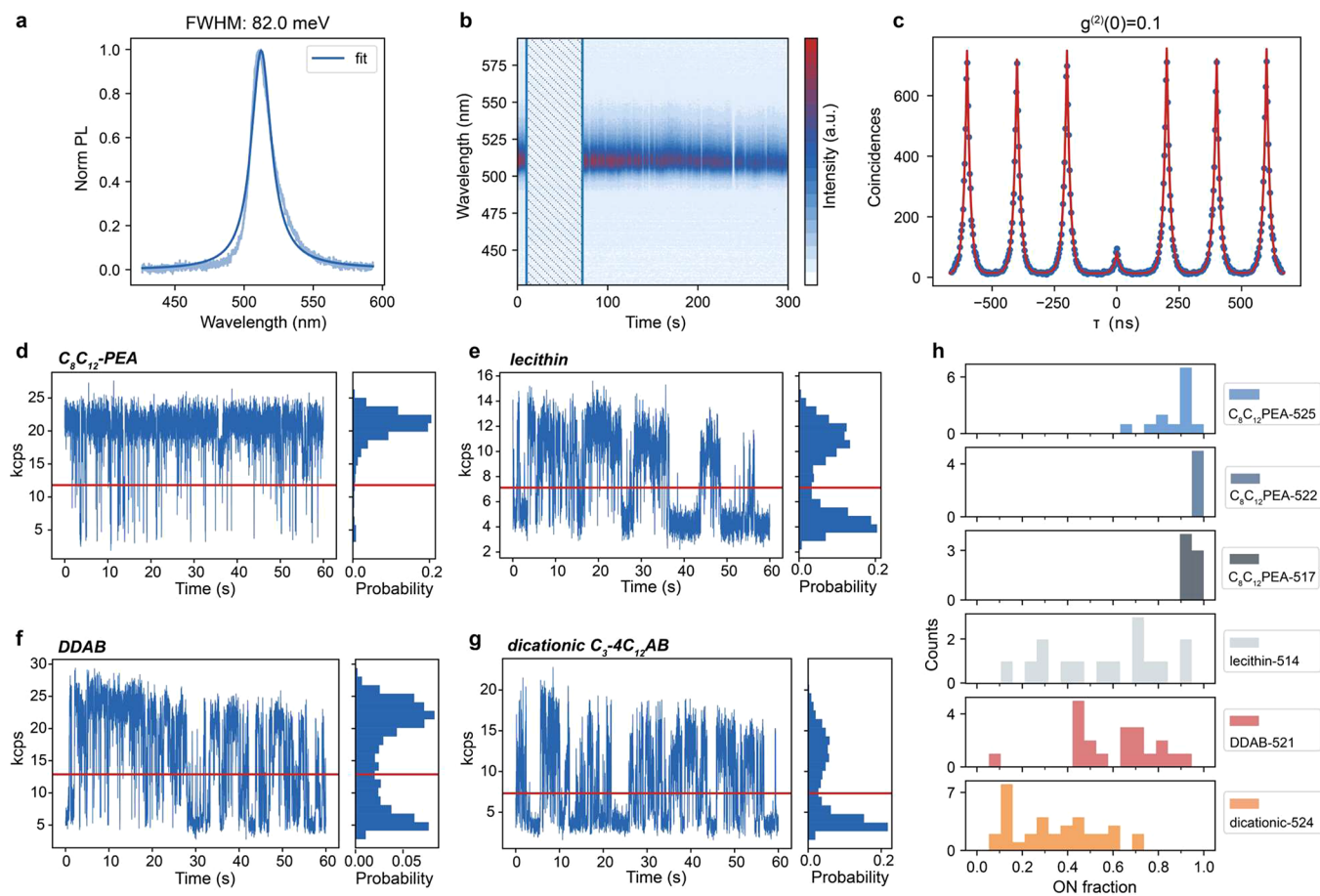


Figure 4. Room-temperature PL of single AZPbBr₃ QDs with various surface capping ligands. (a) PL spectrum of a single C₈C₁₂-PEA-capped AZPbBr₃ QD displaying narrow-band emission with a fwhm of 82 meV. (b) Spectra series of a C₈C₁₂-PEA-capped QD exhibiting spectrally stable PL and small intensity variations. The highlighted time period (shaded area without PL spectral detection) corresponds to the acquisition of the second-order correlation function ($g^{(2)}(t)$), shown in panel (c) and blinking trace by a Hanbury–Brown and Twiss experiment. (c) Second-order photon–photon correlation of a C₈C₁₂-PEA-capped AZPbBr₃ QD displaying high single-photon purity ($g^{(2)}(0) = 0.1$). (d–g) Representative PL blinking traces (10 ms binning time) of a QD capped with branched C₈C₁₂-PEA ligands (panel (d)), lecithin (panel (e)), DDAB (panel (f)), and dicationic amine C₃-4C₁₂AB (panel (g)). (h) Histograms of the fraction of time that single QDs spend in their bright (ON) state. The numbers after the ligand name indicate the ensemble PL central wavelength of the respective sample.

used in the synthesis are fully removed upon washing and do not bind to the NC surfaces.

The presence and integrity of the AZ cation in AZPbBr₃ NCs were characterized with ¹H solid-state NMR spectra (Figure S11a). The bulk material features two main peaks at 4 and 6 ppm. Additional minor species are resolved at 5 and 8 ppm, although the material was phase-pure according to powder XRD (Figure S12). No NMR signal from possible ring-opened alkyl ammonium was detected. The observed species were also found in the AZPbBr₃ NCs in solution and solid-state ¹H measurements, with the addition of the alkyl protons from the ligands at 2 ppm (Figure 3a and Figure S10a). ²⁰⁷Pb solid-state NMR is highly sensitive to deviations from a cubic crystal structure in lead-halide perovskites. Experiments on bulk AZPbBr₃ show a single signal centered at ~485 ppm with a full width at half-maximum (fwhm) of 13.1 kHz, similar to the cubic FAPbBr₃ signal (Figure S11b).⁵¹ The ²⁰⁷Pb solid-state NMR signal for C₈C₁₂-PEA-capped AZPbBr₃ NCs fits very well with the bulk reference, exhibiting a single signal at ~505 ppm with a fwhm of 16.5 kHz (Figure 3c). Broader peaks in NCs, compared to bulk, have previously been

also reported for CsPbBr₃, likely caused by the increased disorder and higher ion mobility.⁵¹

Raman Spectroscopy. Raman spectra of AZPbBr₃ NCs and AZPbBr₃ bulk powders confirmed the presence of the AZ cation within the Pb–Br perovskite cage. Beyond the dense and almost featureless spectrum of bands below 150 cm⁻¹, characteristic for the Pb–Br framework in 3D lead-bromide perovskites,⁵² both NCs and bulk exhibit a band at ~308 cm⁻¹, a doublet at 807 and 871 cm⁻¹, and a band at 1227 cm⁻¹, previously assigned to the AZ-cage mode, ring deformation, and ring stretching, respectively.¹⁵ Only a limited amount of degradation products related to AZ ring opening was detected (Figure S13 and Table S9). Note that some bands remain challenging to assign due to the lack of Raman measurements conducted explicitly on the AZ cation, which is unstable outside the perovskite framework. Notwithstanding these uncertainties, Raman spectroscopy also evidences the AZ cations incorporated in the Pb–Br framework, both in AZPbBr₃ NCs and bulk.

Single-QD Spectroscopy. Room-temperature optical properties of AZPbBr₃ NCs, also referenced here as QDs, due to their quantum-light emission capabilities (vide infra),

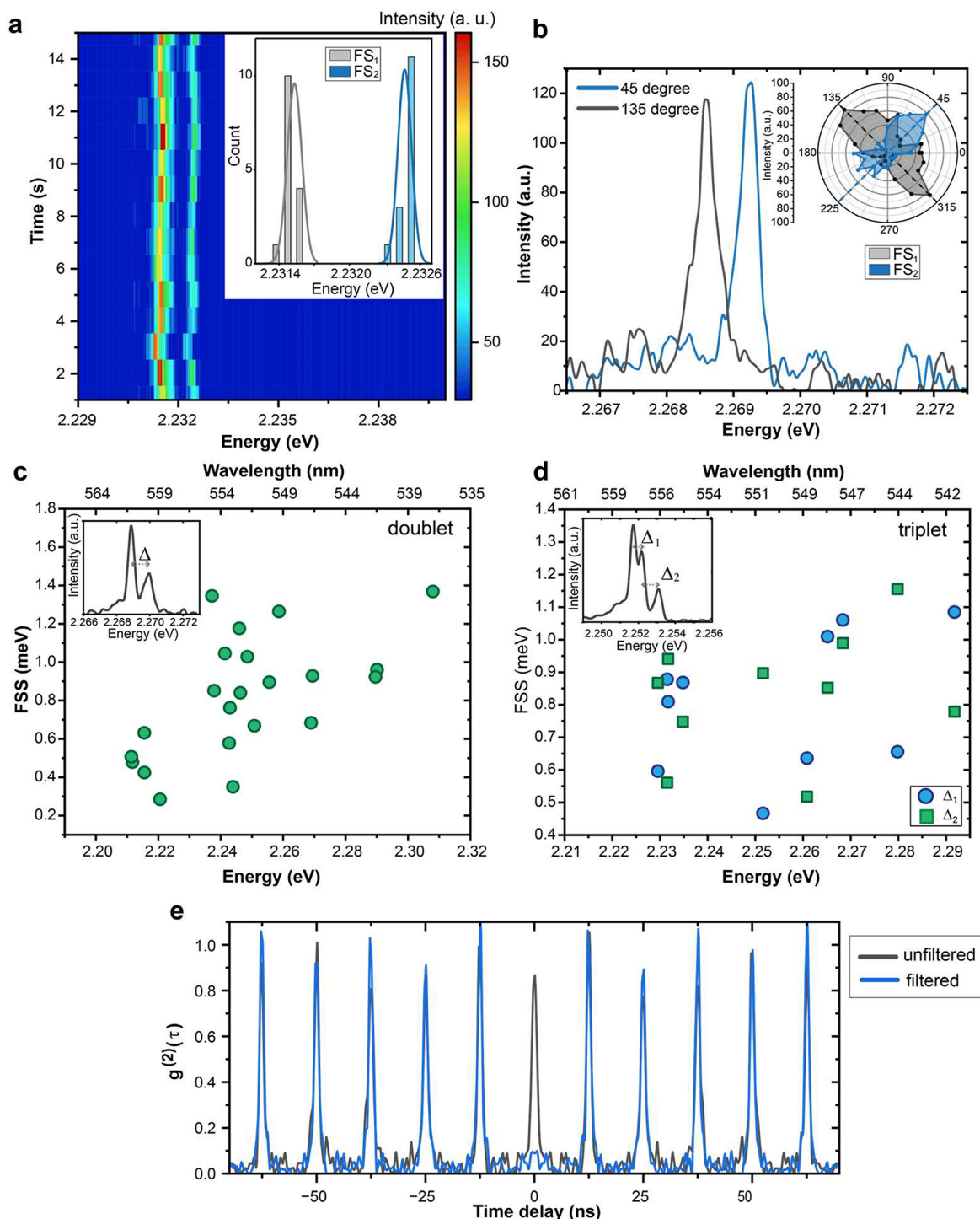


Figure 5. Exciton fine-structure of single AZPbBr₃ QDs at 4 K. (a) Time series of a single QD (1 s integration time and 1800 g/mm grating); sub-meV spectral diffusion allows to resolve the exciton fine structure. This QD exhibits a doublet fine structure with peaks denoted as FS₁ and FS₂. The inset shows an associated histogram of the peak energies (bars), fitted with a Gaussian function (lines). (b) The PL spectra of one single QD measured at two different angles of a linear polarizer in the detection path: 45° (blue) and 135° (gray); this QD has a doublet exciton fine structure. The inset shows a polar plot with the respective PL intensities, as a function of the polarizer angle; both doublet sublevels exhibit highly linear polarization, oriented perpendicular to each other; (c, d) Fine-structure splitting energy (FSS) for all of the single QDs (capped with DDAB or C₈C₁₂-PEA ligands) exhibit doublet sublevels (panel (c)) or triplet sublevels (panel (d)). The insets in panels (c) and (d) show representative spectra for doublet and triplet exciton fine structures, respectively. (e) Second-order correlation function $g^{(2)}(\tau)$ of a single AZPbBr₃ QD under 0.3 $\mu\text{J}/\text{cm}^2$ before (dark gray line) and after (blue line) spectrally filtering out the biexciton emission by a tunable short-pass filter.

were examined via single-particle PL spectroscopy in a home-built inverted oil-immersion microscope (see details in the Supporting Information). Such PL studies at the single-QD

level unveil basic structure–property relationships,⁵³ as well as sample heterogeneities⁵⁴ and temporal fluctuations^{55,56} of emitters, which are otherwise unresolved in the ensemble

spectra. Figure 4a shows a single-particle PL spectrum of an AZPbBr₃ QD capped by C₈C₁₂-PEA ligands. Fitting a Lorentz function to the experimental data returns an emission peak centered at 512 nm and an fwhm of 82 meV, demonstrating the spectrally narrow emission of the individual AZPbBr₃ QDs. Measurements were performed in a nitrogen atmosphere for extended spectral photostability, as evidenced in the PL spectra series in Figure 4b. AZPbBr₃ QDs exhibited high single-photon purity, as confirmed by a strongly suppressed peak at a zero delay time in the second-order photon–photon correlation function $g^{(2)}(t)$ (Figure 4c). The high single-photon purity with $g^{(2)}(0) = 0.1$ is on par with FAPbBr₃ and MAPbBr₃ QDs capped by the same C₈C₁₂-PEA ligand.²⁵

Furthermore, we quantify the PL intensity fluctuations, termed “PL blinking”, i.e., the stochastic switching between a bright (ON) and a dimmed (OFF) state. PL blinking roots in a photoinduced charge trapping at surface defects, possibly mediated by efficient Auger–Meitner recombination, and could be strongly affected by the QD surface passivation.⁵⁷ The fraction of time spent in the ON state (ON fraction) is therefore a suitable metric of the surface quality for the nanomaterial under study at the single-QD level. Recently, we demonstrated that the C₈C₁₂-PEA ligands stabilize hybrid organic–inorganic lead-halide perovskite QDs and enable emission at the single-particle level with >90% ON fraction.²⁵ A blinking trace from a single C₈C₁₂-PEA-capped AZPbBr₃ QD (Figure 4d) also exhibits a high ON fraction (~95%), representative of the high ON fraction (typically >85%) for AZPbBr₃ QDs with this ligand capping (Figure 4h). We then surveyed the blinking behavior of QDs capped by various alternative and post-synthetically attached ligands, i.e., zwitterion lecithin (Figures 4e), monocationic DDAB (Figure 4f), and dicationic C₃-4C₁₂AB (Figure 4g). Although C₈C₁₂-PEA and lecithin are both zwitterionic phospholipids, lecithin-capped QDs exhibit longer OFF events and a significantly smaller ON fraction than those of C₈C₁₂-PEA-capped QDs, symptomatic for the compromised surface passivation of the former. We attribute the superior performance of C₈C₁₂-PEA to the better fit of its primary ammonium binding group into the A-cation site at the QD surface.^{25,30} Likewise, blinking traces of QDs capped by one of the two quaternary ammonium ligands, DDAB or C₃-4C₁₂-AB, displayed ON fractions smaller than those of the C₈C₁₂-PEA-capped QDs. We further observed that all samples, except C₈C₁₂-PEA-capped QDs, feature a large QD-to-QD variation in the ON fraction (Figure 4h). This could be assigned to the sample preparation procedure needed for single-QD spectroscopy, which requires a strong dilution (by a factor of ~50 000) of the colloids.

The dilution step can also alter the QD morphology⁵⁸ and induce a blue shift of the PL energy (Figure S14). Occurring under water-free and inert conditions, structural and optical alterations upon dilution are rationalized considering ligand desorption enhanced by the dynamic ligand binding observed in ionic perovskite QDs.⁵⁹ Dilution-induced alterations can also explain the deviation of ON fractions for the different ligands, despite comparably high PL QYs in the undiluted ensemble (Figure S14). Single-particle spectroscopy thus acts as a stress test for ionic QDs with inherently dynamic ligand binding that is better endured by C₈C₁₂-PEA-capping. The reduced blinking for such a ligand formulation could be exploited for the realization of single-photon sources without the loss in the single-photon purity.⁶⁰

While room-temperature single-QD experiments unveiled the optimal ligand choice, the intrinsic electronic properties of the semiconductor core are probed at cryogenic temperatures. At 4 K, the perturbation by phonons via exciton–phonon coupling is highly suppressed, enabling observation of the exciton fine structure arising from electron–hole exchange interaction as well as emission from exciton complexes. We studied single AZPbBr₃ QDs capped with C₈C₁₂-PEA, DDAB, or lecithin ligands. Single QDs with ensemble QD sizes from ~7–9 nm exhibit exciton PL bands in the range of 2.31–2.20 eV (537–564 nm), with a fwhm ranging from 0.2 to 0.8 meV (where 0.2 meV is our setup resolution). Among the studied ligand systems, only DDAB- and C₈C₁₂-PEA-capped single QDs exhibit a spectrally stable multiline exciton spectrum with sub-meV spectral diffusion (Figure 5a). The multiline spectrum is ascribed to the bright triplet character of excitonic emission in lead-halide perovskites.^{7,61} By introducing a linear polarizer in the collection path and recording the angle-dependent exciton intensities, we obtained the polarization profile typical for a bright triplet exciton: individual exciton sublevels are highly linearly polarized and orthogonal to each other, as in the example displayed in Figure 5b. Across various single QDs, we observed both doublet and triplet exciton fine structures (see insets of Figures 5c and 5d). Splitting energies of doublet (Δ) and triplet (Δ_1 and Δ_2) exciton fine structures are plotted as a function of the exciton energy in Figures 5c and 5d, respectively. Splitting energies vary from 0.2 to 1.4 meV for QDs with PL peak ranging from 2.21 to 2.31 eV. In addition to a systematic trend of increasing splitting energies with increasing exciton energy, large variations in splitting energy are observed for a given exciton energy. This variation was also reported in other lead halide perovskite QDs,^{6,7,61–65} and suggests that the exciton fine-structure splitting is sensitive to the shape anisotropy of the studied QDs. In general, exciton properties of AZPbBr₃ QDs are comparable to CsPbBr₃^{7,66,67} and FAPbBr₃ QDs.^{61,68} Compared to the C₈C₁₂-PEA- or DDAB-capped single QDs, lecithin-capped QDs exhibit stronger spectral diffusion (~10 meV, see Figure S15), consistent with their more-pronounced PL blinking and lower ON fraction at room temperature.

To quantify the quantum correlations among photo-generated exciton complexes, we drive the single QDs under high excitation fluence, hereby obtaining emission also from trion (X^{*}) and biexciton (XX); see one example in Figure S16a. As the excitation fluence increases from 0.003 $\mu\text{J}/\text{cm}^2$ to 0.09 $\mu\text{J}/\text{cm}^2$, two additional peaks emerge on the lower-energy side of the exciton emission spectrum, which are assigned to the trion (red-shifted from E_x by 25 meV) and biexciton (red-shifted from E_x by 40 meV). Summarizing the results from all studied single QDs, binding energies of trion ($\Delta_{X^*} = E_x - E_{X^*}$) and biexciton ($\Delta_{XX} = E_x - E_{XX}$) are plotted as a function of the exciton energies (see Figure S16b). Δ_{X^*} increases from 10 to 25 meV for exciton energies increasing from 2.20 to 2.30 eV, and Δ_{XX} increases from 30 to 40 meV for exciton energies increasing from 2.24 to 2.30 eV. Qualitatively, the observed trend of increasing Δ_{X^*} or Δ_{XX} with increasing exciton energy is universal in semiconductor QDs^{69,70} as the Coulomb interaction among photogenerated charge carriers is steadily enhanced with decreasing QD size. Quantitatively, the size-dependent trends of Δ_{X^*} and Δ_{XX} are similar to those reported for FAPbBr₃ QDs.⁷¹ Utilizing the obtained knowledge of Δ_{XX} in AZPbBr₃ QDs, we performed single-QD antibunching experiments under high excitation fluence (0.3 $\mu\text{J}/\text{cm}^2$) with

and without filtering the biexciton emission. When the spectrum is unfiltered (Figure 5e, dark gray line), no antibunched emission was observed, i.e., $g^{(2)}(0) \approx 1$, suggesting very efficient biexciton emission at 4 K. When the biexciton emission is discarded by spectral filtering (Figure 5e, blue line), emission is characterized by a regular stream of single photons ($g^{(2)}(0) \approx 0$, within the noise floor of ~ 0.1). In addition, all the studied individual AZPbBr₃ QDs feature a monoexponential PL decay with lifetimes between 400 and 1600 ps, as shown in Figure S17. These lifetimes are much longer than reported in CsPbBr₃ QDs, suggesting the absence of a pronounced giant oscillator strength,⁷ probably related to the softer and more dynamic lattice of the AZPbBr₃ QDs. The room-temperature PL decay curves (Figure S18) reveal a reduction in the radiative rates with decreasing NC size. For CsPbBr₃ NCs, such dependence was previously explained by the size-dependent thermal mixing with optically forbidden excitonic transitions.⁷²

CONCLUSIONS

In summary, we have presented a room-temperature colloidal synthesis of monodisperse and quantum-confined AZPbBr₃ NCs with bright emission, size-tunable PL peaks from 498 to 530 nm, and a locally distorted cubic crystal. The stabilization of the AZ cation is confirmed by NMR and Raman spectroscopy. At the single-particle level, AZPbBr₃ QDs capped with DDAB or C₈C₁₂-PEA are as robust as analogously synthesized MAPbBr₃ and FAPbBr₃ QDs reaching high single-photon purity and suppressed blinking behavior at room temperature, and exhibiting bright triplet exciton character of the single-exciton emission at 4 K. This report on the synthesis of colloidal AZPbBr₃ NCs can inspire follow-up investigations of such NCs, for example, further exploring potentials for compositional engineering (mixed cations or anions) and integration into devices such as color enhancers or blue-to-green down-converters.

METHODS

Safety Statement. No unexpected or unusually high safety hazards were encountered.

Synthesis of AZPbBr₃ NCs. Stock Solutions. Aziridine stock solution (0.15 M) was prepared as follows: 15.5 μ L of aziridine was dissolved in 2 mL of anhydrous chloroform and stored in a refrigerator. For PbBr₂-TOPO stock solution (0.04 M), PbBr₂ (1 mmol, 376 mg) and TOPO (5 mmol, 2.15 g) were dissolved in octane (5 mL) at 100 °C, followed by dilution with hexane (20 mL) and filtering through a 0.2 μ L PTFE filter before use. DOPA stock solution (0.57 M) was prepared by dissolving 0.8 mL of DOPA in 3.2 mL hexane. OA stock solution (0.515 M) was prepared by dissolving 0.8 mL of OAc in 3.6 mL of hexane. EtHAc stock solution (0.31 M) was prepared by dissolving 0.2 mL of EtHAc in 3.8 mL of hexane. Erucic acid stock solution (0.56 M) was prepared by dissolving 383 mg of EAc in 2 mL hexane. Alkylphosphonic acid stock solution (alkylPAC, 0.257 M) was prepared by dissolving alkyl phosphonic acid in anhydrous toluene (hexyl-, octyl-, decyl-, or dodecylphosphonic acid). C₁₀PAC and C₁₂PAC dissolve in toluene only upon heating to 80 °C, and the stock solution should be preheated before use. DDAB stock solution (100 mg/mL, 0.215 M) was prepared by dissolving 300 mg of DDAB in 3 mL of anhydrous toluene. C₈C₁₂-PEA stock solution (50 mg/mL) was prepared by dissolving 100 mg of C₈C₁₂-PEA in 2 mL of distilled mesitylene. Lecithin stock solution (50 mg/mL) was prepared by dissolving 200 mg of lecithin in 4 mL hexane. C₃-4C₁₂AB stock solution (100 mg/mL) was prepared by dissolving 100 mg C₃-4C₁₂AB in 1 mL of mesitylene.

Synthesis. In a 25 mL one-neck flask, PbBr₂-TOPO stock solution was combined with additional hexane. Then, a desired volume of DOPA, alkyl-PAC, or OAc (or other carboxylic acids) stock solution was added. Under vigorous stirring (1100 rpm), aziridine in chloroform was swiftly injected into the reaction mixture. After 20 s to 3 min, a stock solution of ligands (DDAB or C₈C₁₂-PEA, lecithin, or C₃-4C₁₂AB) is added to initiate the ligand exchange on the NC surface. Within 2–4 min after the addition of ligands, the crude solution was concentrated by evaporating hexane on a rotary evaporator down to <0.5 mL of residual solvent. The NCs were precipitated from the concentrated colloid by adding nonsolvent. Specific volumes of stock solutions are indicated in Table S1 for all reactions presented in this work.

Purification. For DDAB ligands, NCs were purified using acetone (crude solution:nonsolvent 1:2 (v/v)), followed by solubilization of the obtained NCs in cyclohexane. For C₈C₁₂-PEA ligands, ethyl acetate and acetonitrile mixture (1:1) were used (crude solution:nonsolvent, 1:1 (v/v)), followed by solubilization of the obtained NCs in cyclohexane. For lecithin ligands, ethyl acetate and acetonitrile mixture (1:1) was used (crude solution: nonsolvent, 1:1 (v/v)), followed by solubilization of the obtained NCs in anhydrous toluene. For dicationic C₃-4C₁₂AB ligands, acetone was used as a nonsolvent. In the case of introducing phosphonic acids in the synthesis, first, the crude solution was centrifuged, then a white precipitate was discarded, and the obtained supernatant was concentrated by evaporating on a rotary evaporator down to <0.5 mL of residual solvent, followed by purification with an ethyl acetate/acetone mixture (1:1), and the obtained NCs were dissolved in toluene. Both DDAB and C₈C₁₂-PEA-capped AZPbBr₃ NCs are stable for several months in darkness under ambient conditions. The described synthesis is sensitive to the value of room temperature. Deviation in room temperature (in our case, 21 °C) by 2–3 °C leads to the shift of the PL maximum by 2–4 nm.

Ex-Situ Absorption and PL Spectroscopy. UV-vis absorption spectra were collected using a Jasco Model V770 spectrometer operated in transmission mode. A spectrofluorimeter (Horiba Jobin Yvon, Model Fluoromax 4) that was equipped with a PMT detector was used to acquire steady-state PL spectra from solutions. The excitation wavelength was 400 nm, provided by a 150 W xenon lamp dispersed with a monochromator. Measured intensities were corrected to consider the detector's spectral response. The QY of the solutions was measured with a quantum yield spectrometer (Hamamatsu, Model Quantaury-QY Absolute PL) that was equipped with an integrating sphere. Time-resolved PL traces were acquired in solution by using a FluoTime300 spectrometer from PicoQuant. Samples were excited using a 355 nm detector; the detection was set at the PL peak maximum for each sample.

In-Situ Absorption Setup. The reactions were carried out in a modified commercial cuvette holder (CVH100; Thorlabs). The absorption spectra were recorded in transmission mode with a deuterium-tungsten light source (Ocean Optics, Model DH-2000-BAL-TTL-24 V) and a broad-band spectrometer (OceanInsight, Model HDX-XR). The time resolution in these measurements was set to 50 ms. Custom-developed batch analysis scripts (written in Python) were employed for the data analysis and fitting.

Electron Microscopy Characterization. Transmission electron microscopy (TEM) and scanning transmission electron microscopy (STEM) images were collected by using a JEOL Model JEM-2200FS microscope operated at 200 kV. HR HAADF-STEM was carried out using a probe-aberration-corrected FEI Titan Themis system that was operated at 300 kV, using a beam current of ~ 1 pA. High-resolution images were obtained by summing up 3–5 frames.

SAXS Measurements. SAXS experiments were carried out on a benchtop Bruker Nanostar (Bruker AXS GmbH, Karlsruhe, Germany) using the K α -line of a microfocused X-ray Cu source with a wavelength of 1.5406 Å. The beam was collimated using a 0.3 mm pinhole, leading to a beam diameter of ~ 0.4 mm at the sample position. The sample–detector distance was set to 107 cm and further calibrated with silver behenate, achieving a resolvable q -range of 0.07

$\text{nm}^{-1} \leq q \leq 2.3 \text{ nm}^{-1}$. For selected samples, an additional measurement was performed at a sample-to-detector distance of 27 cm, further calibrated with silver behenate, and combined with previous measurements to obtain an extended q -range of $0.07 \text{ nm}^{-1} \leq q \leq 10 \text{ nm}^{-1}$. The length of the scattering vector \vec{q} is defined as $q = 4\pi \sin 2\theta/\lambda$, where 2θ as the scattering angle and λ the wavelength of the X-ray source; the scattered intensity was recorded on a gaseous avalanche-based detector (VANTEC-2000, Bruker AXS) with 2048×2048 pixels and a pixel size of $68 \mu\text{m} \times 68 \mu\text{m}$. The scattering patterns were recorded at room temperature under moderate vacuum conditions (10^{-2} mbar) to limit air scattering.

Calibration of the scattering vector length q and estimation of the instrumental resolution $\Delta q = 0.25 \text{ nm}^{-1}$ were done by measuring the first diffraction peak of a silver behenate sample and calculating its width. Each sample was sealed in a quartz capillary and mounted in the sample chamber. The scattering intensity was recorded for 700 s for each sample. The intensity of the semitransparent beamstop from empty beam scans was used for transmission calibration. The scattered intensity was extracted, azimuthally averaged, and integrated over each q -value using the Bruker software DIFFRAC.EVA (Bruker AXS, version 4.1). The 1D data was transmission-corrected and background-subtracted from the scattering of the respective solvent, polymers, and the empty quartz capillary using an in-house data pipeline operating under Matlab 2022.

The final scattering pattern was then fitted using the parallelepiped model. For more details, we refer to the section “Small-Angle X-ray Scattering (SAXS) Measurements” in the Supporting Information.

Synchrotron WAXTS Measurements. X-ray total scattering measurements on AZPbBr_3 NCs were performed at the X04SA-MS beamline of the Swiss Light Source (Paul Scherrer Institute, Villigen, Switzerland)⁷³ and at the Swiss–Norwegian beamline (BM01) of the European Synchrotron Radiation Facility (ESRF, Grenoble, France). For more details, we refer to the section “Synchrotron X-ray Total Scattering Measurements” in the Supporting Information.

NMR Measurements. *Solid-State Magic Angle Spinning Nuclear Magnetic Resonance (MAS NMR).* NMR experiments were performed under ambient conditions on a 16.4T Bruker Avance IIIHD spectrometer (Bruker Biospin, Fällanden, Switzerland), that was equipped with a 2.5-mm trippel-channel solid-state probe head. All samples were ground into a fine powder and densely packed into ZrO_2 rotors. The spinning frequency was set to 20 kHz. ^1H , ^{31}P , and ^{207}Pb NMR chemical shifts were externally referenced to TMS, 85% H_3PO_4 in H_2O , and PbMe_4 . The ^1H excitation pulse was set to 2.5 μs . The ^{31}P excitation pulse was set to 5.6 μs , and proton decoupling with a Spinal64 sequence was performed during the detection. For ^{207}Pb , a Hahn echo pulse-sequence was used for all measurements with an echo delay of 0.9 ms. The radio-frequency (rf) field of the echo pulses was set to 19.8 kHz.

Solution NMR. Solution ^1H and ^{31}P NMR spectra were recorded on a 11.7 T Bruker Avance IIIHD spectrometer (Bruker Biospin, Fällanden, Switzerland). The instrument was equipped with a BBO cryogenic probe. The sample temperature was set to 298 K. ^1H spectra were acquired using a one-pulse sequence with a 4 μs excitation pulse and a 1 s recycle delay. ^{31}P spectra were acquired using a one-pulse excitation pulse (14 μs) and proton decoupling with a 2 s recycle delay. All spectra were referenced externally to TMS (^1H) and 85% H_3PO_4 in H_2O (^{31}P).

Powder X-ray Diffraction. Powder X-ray diffraction (XRD) patterns were collected in transmission mode with a STADI P diffractometer (STOE&Cie GmbH) that was equipped with a curved Ge (111) monochromator ($\text{Cu K}\alpha_1 = 1.54056 \text{ \AA}$) and a silicon strip MYTHEN 1K Detector (Fa. DECTRIS). For the measurement, the ground powder was placed between the adhesive tape.

Raman Spectroscopy. Raman spectra were acquired using a Horiba LabRAM HR Evolution confocal microscope. An objective lens (100 \times magnification, 0.9 NA) was used to induce and collect Raman-scattered light from micrometer-scale regions of the samples, using laser excitation at 785 nm (continuous wave, 30 mW). No sample degradation was observed during or after the typical

acquisition time of ~ 25 s. For more details, we refer to the section “Raman Spectroscopy” in the Supporting Information.

Single-QD Spectroscopy. Sample Preparation (Room Temperature). The following steps were performed in a glovebox that is kept under a nitrogen atmosphere and employing dry and filtered octane (Acros Organics, 99+% extra dry), cyclohexane (Acros Organics, 99.5% extra dry), and toluene (Acros Organics, 99.85% extra dry over molecular sieve). AZPbBr_3 NCs were diluted by a factor of 1500–40 000, depending on initial concentration and solvent. Samples were diluted in octane (in the case of $\text{C}_3\text{--}4\text{C}_{12}\text{AB}$ -capped NCs), cyclohexane (in the case of DDAB-capped NCs), or toluene ($\text{C}_8\text{C}_{12}\text{PEA}$ or lecithin-capped NCs). Subsequently, 100 μL of this solution was spin-coated onto a cover glass (Thorlabs, $170 \pm 5 \mu\text{m}$ thickness and 25 mm diameter) at 150 rps for one min or 50 rps for 80 s. The samples were then placed in a home-built sample holder filled with nitrogen to preclude moisture-induced (water and/or oxygen) degradation during the measurements for room temperature experiments.

Room-Temperature Measurements. Room-temperature single-particle fluorescence measurements were performed on a home-built uPL inverted microscope. The setup consists of a 405-nm pulsed laser (PicoQuant, 10 MHz repetition rate, <50 ps pulse width, <100 W/cm²) focused ($1/e^2 = 1 \mu\text{m}$) using an oil immersion objective (1.3 NA) onto the sample mounted on a XYZ-stage (SmarAct). The emitted light is collected by the same objective and passed through a dichroic mirror and a long-pass filter (both 450-nm cut-on wavelength). To record the spectrum, the emitted light is sent to a monochromator coupled to an EMCCD (Princeton Instruments, one frame per second). PL intensity time traces and second-order photon–photon correlations are obtained by sending the emitted light to a Hanbury-Brown and Twiss (HBT) setup consisting of a 50/50 beam splitter, two APDs (Excelitas, 250 ps time resolution), and a TCSPC module (PicoQuant, HydraHarp).

Cryogenic Measurements (at 4 K). For single-QD spectroscopy at 4 K, a home-built micro-PL setup is used. The samples were mounted on XYZ nanopositioning stages inside an evacuated liquid-helium closed-loop cryostat (Montana Instruments) and cooled to a targeted temperature of 4 K. Single NCs were excited using a fiber-coupled excitation laser at an energy of 2.585 eV (480 nm) with a repetition rate of 80 MHz (Toptica, <200 fs pulses), which is focused ($1/e^2$ diameter = 2.4 μm) on the sample by a microscope objective (0.8 NA, 100 \times magnification). Typical energy densities used to excite single NCs were 0.003–0.008 $\mu\text{J}/\text{cm}^2$. The emitted light is collected by the same objective and passed through a dichroic mirror (long-pass, cut-on wavelength of 488 nm) and a long-pass filter at 500 nm. A monochromator (Princeton Instruments, 0.75 m) coupled to a back-illuminated CCD camera is used for spectra measurements. Spectra are measured with a grating featuring 1800 (or 300) lines/mm, blaze 500 nm, resulting in a 0.2 (or 1) meV spectral resolution.

Computational Methods. For details of the computational study, we refer to the section “Computational Methodology” in the Supporting Information.

ASSOCIATED CONTENT

Supporting Information

The Supporting Information is available free of charge at <https://pubs.acs.org/doi/10.1021/acsnano.3c11579>.

Additional details on materials and methods including complete description of the synthetic procedure, TEM and STEM images, Raman spectroscopy measurements, NMR, additional SAXS, WAXTS and single-dot spectroscopy data, and the computational study (PDF)

AUTHOR INFORMATION

Corresponding Authors

Maryna I. Bodnarchuk – Laboratory for Thin Films and Photovoltaics, Empa, Swiss Federal Laboratories for

Materials Science and Technology, Dübendorf 8600, Switzerland; Institute of Inorganic Chemistry, Department of Chemistry and Applied Biosciences, ETH Zürich, Zürich 8093, Switzerland; orcid.org/0000-0001-6597-3266; Email: maryna.bodnarchuk@empa.ch

Maksym V. Kovalenko – Institute of Inorganic Chemistry, Department of Chemistry and Applied Biosciences, ETH Zürich, Zürich 8093, Switzerland; Laboratory for Thin Films and Photovoltaics, Empa, Swiss Federal Laboratories for Materials Science and Technology, Dübendorf 8600, Switzerland; SKKU Institute of Energy Science and Technology (SIEST), Sungkyunkwan University, Suwon 16419, South Korea; orcid.org/0000-0002-6396-8938; Email: mvkovalenko@ethz.ch

Authors

Leon G. Feld – Institute of Inorganic Chemistry, Department of Chemistry and Applied Biosciences, ETH Zürich, Zürich 8093, Switzerland; Laboratory for Thin Films and Photovoltaics, Empa, Swiss Federal Laboratories for Materials Science and Technology, Dübendorf 8600, Switzerland; orcid.org/0000-0001-9755-5085

Chenglian Zhu – Institute of Inorganic Chemistry, Department of Chemistry and Applied Biosciences, ETH Zürich, Zürich 8093, Switzerland; Laboratory for Thin Films and Photovoltaics, Empa, Swiss Federal Laboratories for Materials Science and Technology, Dübendorf 8600, Switzerland

Simon C. Boehme – Institute of Inorganic Chemistry, Department of Chemistry and Applied Biosciences, ETH Zürich, Zürich 8093, Switzerland; Laboratory for Thin Films and Photovoltaics, Empa, Swiss Federal Laboratories for Materials Science and Technology, Dübendorf 8600, Switzerland; orcid.org/0000-0002-8399-5773

Federica Bertolotti – Department of Science and High Technology and To.Sca.Lab., University of Insubria, Como 22100, Italy; orcid.org/0000-0002-6001-9040

Jonathan Avaro – Centre for X-ray Analytics & Laboratory for Biomimetic Membranes and Textiles, Empa, Swiss Federal Laboratories for Materials Science and Technology, St. Gallen 9014, Switzerland; orcid.org/0000-0001-6596-3228

Marcel Aebli – Institute of Inorganic Chemistry, Department of Chemistry and Applied Biosciences, ETH Zürich, Zürich 8093, Switzerland; Laboratory for Thin Films and Photovoltaics, Empa, Swiss Federal Laboratories for Materials Science and Technology, Dübendorf 8600, Switzerland

Showkat Hassan Mir – Materials Theory for Energy Scavenging (MATES) Lab, Harish-Chandra Research Institute (HRI) Allahabad, A C.I. of Homi Bhabha National Institute (HBNI), Jhansi, Prayagraj (Allahabad) 211019, India; orcid.org/0000-0002-9291-4680

Norberto Masciocchi – Department of Science and High Technology and To.Sca.Lab., University of Insubria, Como 22100, Italy; orcid.org/0000-0001-9921-2350

Rolf Erni – Electron Microscopy Center, Empa, Swiss Federal Laboratories for Materials Science and Technology, Dübendorf 8600, Switzerland; orcid.org/0000-0003-2391-5943

Sudip Chakraborty – Materials Theory for Energy Scavenging (MATES) Lab, Harish-Chandra Research Institute (HRI) Allahabad, A C.I. of Homi Bhabha National Institute

(HBNI), Jhansi, Prayagraj (Allahabad) 211019, India;

orcid.org/0000-0002-6765-2084

Antonietta Guagliardi – Istituto di Cristallografia and To.Sca.Lab, Consiglio Nazionale delle Ricerche, Como 22100, Italy; orcid.org/0000-0001-6390-2114

Gabriele Rainò – Institute of Inorganic Chemistry, Department of Chemistry and Applied Biosciences, ETH Zürich, Zürich 8093, Switzerland; Laboratory for Thin Films and Photovoltaics, Empa, Swiss Federal Laboratories for Materials Science and Technology, Dübendorf 8600, Switzerland; orcid.org/0000-0002-2395-4937

Complete contact information is available at: <https://pubs.acs.org/10.1021/acsnano.3c11579>

Notes

This manuscript has been submitted to a preprint server: Bodnarchuk, M. I.; Feld, L. G.; Zhu, C.; et al. Colloidal aziridinium lead bromide quantum dots. *Research Square*, 2023, [10.21203/rs.3.rs-3671642/v1](https://doi.org/10.21203/rs.3.rs-3671642/v1) (accessed November 29, 2023).

The authors declare no competing financial interest.

ACKNOWLEDGMENTS

This work was supported by the Swiss National Science Foundation (Grant No. 200021_192308, project Q-Light) and, in part, by the European Union through Horizon 2020 Research and Innovation Programme (ERC CoG Grant, Grant Agreement No. 819740, Project No. SCALE-HALO) and by the Air Force Office of Scientific Research (under Award No. FA8655-21-1-7013). A.G. acknowledges partial funding from project PE0000021, “Network 4 Energy Sustainable Transition-NEST”, Spoke 1, funded by European Union-NextGenerationEU under NRRP, Mission 4, Component 2, Investment 1.3-Call for tender No. 1561 of Ministero dell'Università e della Ricerca (MUR). Antonio Cervellino and the technical staff of the MS-X04SA beamline of the Swiss Light Source (Paul Scherrer Institute, Switzerland) are acknowledged for the room-temperature synchrotron measurements on AZPbBr₃, as colloidal suspensions of NCs and bulk powder. Dmitry Chernyshov and the technical staff of the Swiss-Norwegian Beamline (BM01) of the European Synchrotron Radiation Facility (ESRF, France) are acknowledged for the technical assistance during the RT and temperature-dependent experiment on AZPbBr₃ NCs. Amrutha Rajan is acknowledged for assistance with PLQY measurements.

REFERENCES

- (1) Dey, A.; Ye, J.; De, A.; Debroye, E.; Ha, S. K.; Bladt, E.; Kshirsagar, A. S.; Wang, Z.; Yin, J.; Wang, Y.; et al. State of the Art and Prospects for Halide Perovskite Nanocrystals. *ACS Nano* 2021, 15, 10775–10981.
- (2) Akkerman, Q. A.; Rainò, G.; Kovalenko, M. V.; Manna, L. Genesis, Challenges and Opportunities for Colloidal Lead Halide Perovskite Nanocrystals. *Nat. Mater.* 2018, 17, 394–405.
- (3) Kovalenko, M. V.; Protesescu, L.; Bodnarchuk, M. I. Properties and Potential optoelectronic Applications of Lead Halide Perovskite Nanocrystals. *Science* 2017, 358, 745–750.
- (4) Protesescu, L.; Yakunin, S.; Bodnarchuk, M. I.; Krieg, F.; Caputo, R.; Hendon, C. H.; Yang, R. X.; Walsh, A.; Kovalenko, M. V. Nanocrystals of Cesium Lead Halide Perovskites (CsPbX₃, X = Cl, Br, and I): Novel Optoelectronic Materials Showing Bright Emission with Wide Color Gamut. *Nano Lett.* 2015, 15, 3692–3696.
- (5) Rainò, G.; Nedelcu, G.; Protesescu, L.; Bodnarchuk, M. I.; Kovalenko, M. V.; Mahrt, R. F.; Stöferle, T. Single Cesium Lead

- Halide Perovskite Nanocrystals at Low Temperature: Fast Single-Photon Emission, Reduced Blinking, and Exciton Fine Structure. *ACS Nano* **2016**, *10*, 2485–2490.
- (6) Utzat, H.; Sun, W.; Kaplan, A. E. K.; Krieg, F.; Ginterseder, M.; Spokoiny, B.; Klein, N. D.; Shulenberger, K. E.; Perkinson, C. F.; Kovalenko, M. V.; Bawendi, M. G. Coherent Single-Photon Emission from Colloidal Lead Halide Perovskite Quantum Dots. *Science* **2019**, *363*, 1068–1072.
- (7) Becker, M. A.; Vaxenburg, R.; Nedelcu, G.; Sercel, P. C.; Shabaev, A.; Mehl, M. J.; Michopoulos, J. G.; Lambrakos, S. G.; Bernstein, N.; Lyons, J. L.; Stöferle, T.; Mahrt, R. F.; Kovalenko, M. V.; Norris, D. J.; Rainò, G.; Efros, A. L. Bright Triplet Excitons in Caesium Lead Halide Perovskites. *Nature* **2018**, *553*, 189–193.
- (8) Protesescu, L.; Yakunin, S.; Kumar, S.; Bär, J.; Bertolotti, F.; Masciocchi, N.; Guagliardi, A.; Grotevent, M.; Shorubalko, I.; Bodnarchuk, M. I.; Shih, C.-J.; Kovalenko, M. V. Dismantling the “Red Wall” of Colloidal Perovskites: Highly Luminescent Formamidinium and Formamidinium–Cesium Lead Iodide Nanocrystals. *ACS Nano* **2017**, *11*, 3119–3134.
- (9) Saliba, M.; Matsui, T.; Seo, J.-Y.; Domanski, K.; Correa-Baena, J.-P.; Nazeeruddin, M. K.; Zakeeruddin, S. M.; Tress, W.; Abate, A.; Hagfeldt, A.; Grätzel, M. Cesium-Containing Triple Cation Perovskite Solar Cells: Improved Stability, Reproducibility and High Efficiency. *Energy Environ. Sci.* **2016**, *9*, 1989–1997.
- (10) Liu, Y.; Zhang, Y.; Zhu, X.; Yang, Z.; Ke, W.; Feng, J.; Ren, X.; Zhao, K.; Liu, M.; Kanatzidis, M. G.; Liu, S. Inch-Sized High-Quality Perovskite Single Crystals by Suppressing Phase Segregation for Light-Powered Integrated Circuits. *Sci. Adv.* **2021**, *7*, eabc8844.
- (11) Otero-Martínez, C.; Imran, M.; Schrenker, N. J.; Ye, J.; Ji, K.; Rao, A.; Stranks, S. D.; Hoye, R. L. Z.; Bals, S.; Manna, L.; Pérez-Juste, J.; Polavarapu, L. Fast A-Site Cation Cross-Exchange at Room Temperature: Single-to Double- and Triple-Cation Halide Perovskite Nanocrystals. *Angew. Chem., Int. Ed.* **2022**, *61*, e202205617.
- (12) Lignos, I.; Morad, V.; Shynkarenko, Y.; Bernasconi, C.; Maceiczyn, R. M.; Protesescu, L.; Bertolotti, F.; Kumar, S.; Ochsenein, S. T.; Masciocchi, N.; Guagliardi, A.; Shih, C.-J.; Bodnarchuk, M. I.; deMello, A. J.; Kovalenko, M. V. Exploration of Near-Infrared-Emissive Colloidal Multinary Lead Halide Perovskite Nanocrystals Using an Automated Microfluidic Platform. *ACS Nano* **2018**, *12*, 5504–5517.
- (13) Petsova, H. R.; Kucheriv, O. I.; Shova, S.; Gural'skiy, I. A. Aziridinium Cation Templating 3D Lead Halide Hybrid Perovskites. *Chem. Commun.* **2022**, *58*, 5745–5748.
- (14) Semenikhin, O. A.; Kucheriv, O. I.; Sacarescu, L.; Shova, S.; Gural'skiy, I. A. Quantum Dots Assembled from an Aziridinium Based Hybrid Perovskite Displaying Tunable Luminescence. *Chem. Commun.* **2023**, *59*, 3566–3569.
- (15) Stefańska, D.; Ptak, M.; Mączka, M. Synthesis, Photoluminescence and Vibrational Properties of Aziridinium Lead Halide Perovskites. *Molecules* **2022**, *27*, 7949.
- (16) Ren, K.; Zheng, C.; Brook, M. A.; Rubel, O. Stability of Aziridinium Lead Iodide Perovskite: Ring Strain and Water Vulnerability. arXiv 2019, arXiv:1908.10462.
- (17) Banks, H. D. The Profound Effect of Fluorine Substitution on the Reactivity and Regioselectivity of Nucleophilic Substitution Reactions of Strained Heterocycles. A Study of Aziridine and Its Derivatives. *J. Org. Chem.* **2006**, *71*, 8089–8097.
- (18) Cox, J. D.; Pilcher, G. *Thermochemistry of Organic and Organometallic Compounds*, Vol. 74; Academic Press: London and New York, 1970; 727 pp.
- (19) Zheng, C.; Rubel, O. Aziridinium Lead Iodide: a Stable, Low-Band-Gap Hybrid Halide Perovskite for Photovoltaics. *J. Phys. Chem. Lett.* **2018**, *9*, 874–880.
- (20) Zheng, C.; Rubel, O. Ionization Energy as a Stability Criterion for Halide Perovskites. *J. Phys. Chem. C* **2017**, *121*, 11977–11984.
- (21) Teng, Q.; Shi, T.; Zhao, Y.-J. First-Principles Study of Aziridinium Lead Iodide Perovskite for Photovoltaics. *ChemPhysChem* **2019**, *20*, 602–607.
- (22) Teng, Q.; Shi, T.; Liao, C.; Zhao, Y.-J. First-Principles Study of Aziridinium Tin Iodide Perovskites for Photovoltaics. *J. Mater. Chem. C* **2021**, *9*, 982–990.
- (23) Weckhuysen, B. M.; Kitagawa, S.; Tsapatsis, M. Reactions in Confined Spaces. *ChemPhysChem* **2018**, *19*, 339–340.
- (24) Akkerman, Q. A.; Nguyen, T. P. T.; Boehme, S. C.; Montanarella, F.; Dirin, D. N.; Wechsler, P.; Beiglböck, F.; Rainò, G.; Erni, R.; Katan, C.; Even, J.; Kovalenko, M. V. Controlling the Nucleation and Growth Kinetics of Lead Halide Perovskite Quantum Dots. *Science* **2022**, *377*, 1406–1412.
- (25) Morad, V.; Stelmakh, A.; Svyrydenko, M.; et al. Designer Phospholipid Capping Ligands for Soft Metal Halide Nanocrystals. *Nature* **2023**, DOI: 10.1038/s41586-023-06932-6.
- (26) Bodnarchuk, M. I.; Boehme, S. C.; ten Brinck, S.; Bernasconi, C.; Shynkarenko, Y.; Krieg, F.; Widmer, R.; Aeschlimann, B.; Günther, D.; Kovalenko, M. V.; Infante, I. Rationalizing and Controlling the Surface Structure and Electronic Passivation of Cesium Lead Halide Nanocrystals. *ACS Energy Lett.* **2019**, *4*, 63–74.
- (27) Pan, J.; Quan, L. N.; Zhao, Y.; Peng, W.; Murali, B.; Sarmah, S. P.; Yuan, M.; Sinatra, L.; Alyami, N. M.; Liu, J.; Yassitepe, E.; Yang, Z.; Voznyy, O.; Comin, R.; Hedhili, M. N.; Mohammed, O. F.; Lu, Z. H.; Kim, D. H.; Sargent, E. H.; Bakr, O. M. Highly Efficient Perovskite-Quantum-Dot Light-Emitting Diodes by Surface Engineering. *Adv. Mater.* **2016**, *28*, 8718–8725.
- (28) Krieg, F.; Ong, Q. K.; Burian, M.; Rainò, G.; Naumenko, D.; Amenitsch, H.; Süess, A.; Grotevent, M. J.; Krumeich, F.; Bodnarchuk, M. I.; Shorubalko, I.; Stellacci, F.; Kovalenko, M. V. Stable Ultraconcentrated and Ultradilute Colloids of CsPbX₃ (X = Cl, Br) Nanocrystals Using Natural Lecithin as a Capping Ligand. *J. Am. Chem. Soc.* **2019**, *141*, 19839–19849.
- (29) Imran, M.; Ijaz, P.; Goldoni, L.; Maggioni, D.; Petralanda, U.; Prato, M.; Almeida, G.; Infante, I.; Manna, L. Simultaneous Cationic and Anionic Ligand Exchange for Colloidally Stable CsPbBr₃ Nanocrystals. *ACS Energy Lett.* **2019**, *4*, 819–824.
- (30) Stelmakh, A.; Aebli, M.; Baumketner, A.; Kovalenko, M. V. On the Mechanism of Alkylammonium Ligands Binding to the Surface of CsPbBr₃ Nanocrystals. *Chem. Mater.* **2021**, *33*, 5962–5973.
- (31) Ginterseder, M.; Sun, W.; Shcherbakov-Wu, W.; McIsaac, A. R.; Berkinsky, D. B.; Kaplan, A. E. K.; Wang, L.; Krajewska, C.; Šverko, T.; Perkinson, C. F.; Utzat, H.; Tisdale, W. A.; Van Voorhis, T.; Bawendi, M. G. Lead Halide Perovskite Nanocrystals with Low Inhomogeneous Broadening and High Coherent Fraction Through Dicationic Ligand Engineering. *Nano Lett.* **2023**, *23*, 1128–1134.
- (32) Aubert, T.; Golovatenko, A. A.; Samoli, M.; Lermusiaux, L.; Zinn, T.; Abécassis, B.; Rodina, A. V.; Hens, Z. General Expression for the Size-Dependent Optical Properties of Quantum Dots. *Nano Lett.* **2022**, *22*, 1778–1785.
- (33) Yang, Z.; Surrente, A.; Galkowski, K.; Miyata, A.; Portugall, O.; Sutton, R. J.; Haghighirad, A. A.; Snaith, H. J.; Maude, D. K.; Plochocka, P.; Nicholas, R. J. Impact of the Halide Cage on the Electronic Properties of Fully Inorganic Cesium Lead Halide Perovskites. *ACS Energy Lett.* **2017**, *2*, 1621–1627.
- (34) Bertolotti, F.; Dengo, N.; Cervellino, A.; Bodnarchuk, M. I.; Bernasconi, C.; Cherniukh, I.; Berezovska, Y.; Boehme, S. C.; Kovalenko, M. V.; Masciocchi, N.; Guagliardi, A. Size- and Temperature-Dependent Lattice Anisotropy and Structural Distortion in CsPbBr₃ Quantum Dots by Reciprocal Space X-ray Total Scattering Analysis. *Small Struct.* **2023**, 2300264.
- (35) Mannino, G.; Deretzis, I.; Smecca, E.; La Magna, A.; Alberti, A.; Ceratti, D.; Cahen, D. Temperature-Dependent Optical Band Gap in CsPbBr₃, MAPbBr₃, and FAPbBr₃ Single Crystals. *J. Phys. Chem. Lett.* **2020**, *11*, 2490–2496.
- (36) Reuveni, G.; Diskin-Posner, Y.; Gehrman, C.; Godse, S.; Gkikas, G. G.; Buchine, I.; Aharon, S.; Korobko, R.; Stoumpos, C. C.; Egger, D. A.; Yaffe, O. Static and Dynamic Disorder in Formamidinium Lead Bromide Single Crystals. *J. Phys. Chem. Lett.* **2023**, *14*, 1288–1293.
- (37) Weadock, N. J.; Sterling, T. C.; Vigil, J. A.; Gold-Parker, A.; Smith, I. C.; Ahammed, B.; Krogstad, M. J.; Ye, F.; Voneshen, D.;

- Gehring, P. M.; Rappe, A. M.; Steinrück, H.-G.; Ertekin, E.; Karunadasa, H. I.; Reznik, D.; Toney, M. F. The Nature of Dynamic Local Order in $\text{CH}_3\text{NH}_3\text{PbI}_3$ and $\text{CH}_3\text{NH}_3\text{PbBr}_3$. *Joule* **2023**, *7*, 1051–1066.
- (38) Comin, R.; Crawford, M. K.; Said, A. H.; Herron, N.; Guise, W. E.; Wang, X.; Whitfield, P. S.; Jain, A.; Gong, X.; McGaughey, A. J. H.; Sargent, E. H. Lattice Dynamics and the Nature of Structural Transitions in Organolead Halide Perovskites. *Phys. Rev. B* **2016**, *94*, 094301.
- (39) Carignano, M. A.; Aravindh, S. A.; Roqan, I. S.; Even, J.; Katan, C. Critical Fluctuations and Anharmonicity in Lead Iodide Perovskites from Molecular Dynamics Supercell Simulations. *J. Phys. Chem. C* **2017**, *121*, 20729–20738.
- (40) Beecher, A. N.; Semonin, O. E.; Skelton, J. M.; Frost, J. M.; Terban, M. W.; Zhai, H.; Alatas, A.; Owen, J. S.; Walsh, A.; Billinge, S. J. L. Direct Observation of Dynamic Symmetry Breaking Above Room Temperature in Methylammonium Lead Iodide Perovskite. *ACS Energy Lett.* **2016**, *1*, 880–887.
- (41) Hanusch, F. C.; Wiesenmayer, E.; Mankel, E.; Binek, A.; Angloher, P.; Fraunhofer, C.; Giesbrecht, N.; Feckl, J. M.; Jaegermann, W.; Johrendt, D.; Bein, T.; Docampo, P. Efficient Planar Heterojunction Perovskite Solar Cells Based on Formamidinium Lead Bromide. *J. Phys. Chem. Lett.* **2014**, *5*, 2791–2795.
- (42) Protesescu, L.; Yakunin, S.; Bodnarchuk, M. I.; Bertolotti, F.; Masciocchi, N.; Guagliardi, A.; Kovalenko, M. V. Monodisperse Formamidinium Lead Bromide Nanocrystals with Bright and Stable Green Photoluminescence. *J. Am. Chem. Soc.* **2016**, *138*, 14202–14205.
- (43) Dirin, D. N.; Vivani, A.; Zacharias, M.; Sekh, T. V.; Cherniukh, I.; Yakunin, S.; Bertolotti, F.; Aebli, M.; Schaller, R. D.; Wiczorek, A.; Siol, S.; Cancellieri, C.; Jeurgens, L. P. H.; Masciocchi, N.; Guagliardi, A.; Pedesseau, L.; Even, J.; Kovalenko, M. V.; Bodnarchuk, M. I. Intrinsic Formamidinium tin Iodide Nanocrystals by Suppressing the Sn(IV) Impurities. *Nano Lett.* **2023**, *23*, 1914–1923.
- (44) Bertolotti, F.; Protesescu, L.; Kovalenko, M. V.; Yakunin, S.; Cervellino, A.; Billinge, S. J. L.; Terban, M. W.; Pedersen, J. S.; Masciocchi, N.; Guagliardi, A. Coherent nanotwins and dynamic disorder in cesium lead halide perovskite nanocrystals. *ACS Nano* **2017**, *11*, 3819–3831.
- (45) Boehme, S. C.; Bodnarchuk, M. I.; Burian, M.; Bertolotti, F.; Cherniukh, I.; Bernasconi, C.; Zhu, C.; Erni, R.; Amenitsch, H.; Naumenko, D.; Andrusiv, H.; Semkiv, N.; John, R. A.; Baldwin, A.; Galkowski, K.; Masciocchi, N.; Stranks, S. D.; Rainò, G.; Guagliardi, A.; Kovalenko, M. V. Strongly Confined CsPbBr_3 Quantum Dots as Quantum Emitters and Building Blocks for Rhombic Superlattices. *ACS Nano* **2023**, *17*, 2089–2100.
- (46) Zhao, Q.; Hazarika, A.; Schelhas, L. T.; Liu, J.; Gaubing, E. A.; Li, G.; Zhang, M.; Toney, M. F.; Sercel, P. C.; Luther, J. M. Size-Dependent Lattice Structure and Confinement Properties in CsPbI_3 perovskite Nanocrystals: Negative Surface Energy for Stabilization. *ACS Energy Lett.* **2020**, *5*, 238–247.
- (47) Goldschmidt, V. M. Die Gesetze der Krystallochemie. *Naturwissenschaften* **1926**, *14*, 477–485.
- (48) Li, W.; Wang, Z.; Deschler, F.; Gao, S.; Friend, R. H.; Cheetham, A. K. Chemically Diverse and Multifunctional Hybrid Organic–Inorganic Perovskites. *Nat. Rev. Mater.* **2017**, *2*, 16099.
- (49) Bartel, C. J.; Sutton, C.; Goldsmith, B. R.; Ouyang, R.; Musgrave, C. B.; Ghiringhelli, L. M.; Scheffler, M. New Tolerance Factor to Predict the Stability of Perovskite Oxides and Halides. *Sci. Adv.* **2019**, *5*, eaav0693.
- (50) Wang, F.; Tang, R.; Kao, J. L. F.; Dingman, S. D.; Buhro, W. E. Spectroscopic Identification of Tri-*n*-Octylphosphine Oxide (TOPO) Impurities and Elucidation of Their Roles in Cadmium Selenide Quantum-Wire Growth. *J. Am. Chem. Soc.* **2009**, *131*, 4983–4994.
- (51) Aebli, M.; Piveteau, L.; Nazarenko, O.; Benin, B. M.; Krieg, F.; Verel, R.; Kovalenko, M. V. Lead-Halide Scalar Couplings in 207Pb NMR of APbX_3 Perovskites (A = Cs, Methylammonium, Formamidinium; X = Cl, Br, I). *Sci. Rep.* **2020**, *10*, 8229.
- (52) Kontos, A. G.; Manolis, G. K.; Kaltzoglou, A.; Palles, D.; Kamitsos, E. I.; Kanatzidis, M. G.; Falaras, P. Halogen– NH_2^+ Interaction, Temperature-Induced Phase Transition, and Ordering in $(\text{NH}_2\text{CHNH}_2)_2\text{PbX}_3$ (X = Cl, Br, I) Hybrid Perovskite. *J. Phys. Chem. C* **2020**, *124*, 8479–8487.
- (53) Zhou, J.; Chizhik, A. I.; Chu, S.; Jin, D. Single-Particle Spectroscopy for Functional Nanomaterials. *Nature* **2020**, *579*, 41–50.
- (54) Galland, C.; Ghosh, Y.; Steinbrück, A.; Sykora, M.; Hollingsworth, J. A.; Klimov, V. I.; Htoon, H. Two Types of Luminescence Blinking Revealed by Spectroelectrochemistry of Single Quantum Dots. *Nature* **2011**, *479*, 203–207.
- (55) Nirmal, M.; Dabbousi, B. O.; Bawendi, M. G.; Macklin, J. J.; Trautman, J. K.; Harris, T. D.; Brus, L. E. Fluorescence Intermittency in Single Cadmium Selenide Nanocrystals. *Nature* **1996**, *383*, 802–804.
- (56) Basché, T.; Moerner, W. E.; Orrit, M.; Talon, H. Photon Antibunching in the Fluorescence of a Single Dye Molecule Trapped in a Solid. *Phys. Rev. Lett.* **1992**, *69*, 1516–1519.
- (57) Chen, O.; Zhao, J.; Chauhan, V. P.; Cui, J.; Wong, C.; Harris, D. K.; Wei, H.; Han, H.-S.; Fukumura, D.; Jain, R. K.; Bawendi, M. G. Compact High-Quality CdSe–CdS Core–Shell Nanocrystals with Narrow Emission Linewidths and Suppressed Blinking. *Nat. Mater.* **2013**, *12*, 445–451.
- (58) Rainò, G.; Yazdani, N.; Boehme, S. C.; Kober-Czerny, M.; Zhu, C.; Krieg, F.; Rossell, M. D.; Erni, R.; Wood, V.; Infante, I.; Kovalenko, M. V. Ultra-Narrow Room-Temperature Emission from Single CsPbBr_3 Perovskite Quantum Dots. *Nat. Commun.* **2022**, *13*, 2587.
- (59) De Roo, J.; Ibáñez, M.; Geiregat, P.; Nedelcu, G.; Walravens, W.; Maes, J.; Martins, J. C.; Van Driessche, I.; Kovalenko, M. V.; Hens, Z. Highly Dynamic Ligand Binding and Light Absorption Coefficient of Cesium Lead Bromide Perovskite Nanocrystals. *ACS Nano* **2016**, *10*, 2071–2081.
- (60) Park, Y.-S.; Lim, J.; Klimov, V. I. Asymmetrically Strained Quantum Dots with Non-Fluctuating Single-Dot Emission Spectra and Subthermal Room-Temperature Linewidths. *Nat. Mater.* **2019**, *18*, 249–255.
- (61) Tamarat, P.; Bodnarchuk, M. I.; Trebbia, J.-B.; Erni, R.; Kovalenko, M. V.; Even, J.; Lounis, B. The Ground Exciton State of Formamidinium Lead Bromide Perovskite Nanocrystals is a Singlet Dark State. *Nat. Mater.* **2019**, *18*, 717–724.
- (62) Tamarat, P.; Hou, L.; Trebbia, J.-B.; Swarnkar, A.; Biadala, L.; Louyer, Y.; Bodnarchuk, M. I.; Kovalenko, M. V.; Even, J.; Lounis, B. The Dark Exciton Ground State Promotes Photon-Pair Emission in Individual Perovskite Nanocrystals. *Nat. Commun.* **2020**, *11*, 6001.
- (63) Yin, C.; Chen, L.; Song, N.; Lv, Y.; Hu, F.; Sun, C.; Yu, W. W.; Zhang, C.; Wang, X.; Zhang, Y.; Xiao, M. Bright-Exciton Fine-Structure Splittings in Single Perovskite Nanocrystals. *Phys. Rev. Lett.* **2017**, *119*, 026401.
- (64) Cho, K.; Tahara, H.; Yamada, T.; Suzuura, H.; Tadano, T.; Sato, R.; Saruyama, M.; Hirori, H.; Teranishi, T.; Kanemitsu, Y. Exciton–Phonon and Trion–Phonon Couplings Revealed by Photoluminescence Spectroscopy of Single CsPbBr_3 Perovskite Nanocrystals. *Nano Lett.* **2022**, *22*, 7674–7681.
- (65) Amara, M.-R.; Said, Z.; Huo, C.; Pierret, A.; Voisin, C.; Gao, W.; Xiong, Q.; Diederichs, C. Spectral Fingerprint of Quantum Confinement in Single CsPbBr_3 Nanocrystals. *Nano Lett.* **2023**, *23*, 3607–3613.
- (66) Fu, M.; Tamarat, P.; Huang, H.; Even, J.; Rogach, A. L.; Lounis, B. Neutral and Charged Exciton Fine Structure in Single Lead Halide Perovskite Nanocrystals Revealed by Magneto-Optical Spectroscopy. *Nano Lett.* **2017**, *17*, 2895–2901.
- (67) Guilloux, V.; Ghribi, A.; Majrab, S.; Margailan, F.; Bernard, M.; Bernardot, F.; Legrand, L.; Lhuillier, E.; Boujdaria, K.; Chamarro, M.; Testelin, C.; Barisien, T. Exciton Fine Structure of CsPbCl_3 Nanocrystals: an Interplay of Electron–Hole Exchange Interaction, Crystal Structure, Shape Anisotropy, and Dielectric Mismatch. *ACS Nano* **2023**, *17*, 12266–12277.

(68) Pfingsten, O.; Klein, J.; Protesescu, L.; Bodnarchuk, M. I.; Kovalenko, M. V.; Bacher, G. Phonon Interaction and Phase Transition in Single Formamidinium Lead Bromide Quantum Dots. *Nano Lett.* **2018**, *18*, 4440–4446.

(69) Zhu, C.; Nguyen, T.; Boehme, S. C.; Moskalenko, A.; Dirin, D. N.; Bodnarchuk, M. I.; Katan, C.; Even, J.; Rainò, G.; Kovalenko, M. V. Many-Body Correlations and Exciton Complexes in CsPbBr₃ Quantum Dots. *Adv. Mater.* **2023**, *35*, 2208354.

(70) Tamarat, P.; Prin, E.; Berezovska, Y.; Moskalenko, A.; Nguyen, T. P. T.; Xia, C.; Hou, L.; Trebbia, J.-B.; Zacharias, M.; Pedesseau, L.; et al. Universal Scaling Laws for Charge-Carrier interactions with Quantum Confinement in lead-Halide Perovskites. *Nat. Commun.* **2023**, *14*, 229.

(71) Cho, K.; Yamada, T.; Tahara, H.; Tadano, T.; Suzuura, H.; Saruyama, M.; Sato, R.; Teranishi, T.; Kanemitsu, Y. Luminescence Fine Structures in Single Lead Halide Perovskite Nanocrystals: Size Dependence of the Exciton–Phonon Coupling. *Nano Lett.* **2021**, *21*, 7206–7212.

(72) Krieg, F.; Sercel, P. C.; Burian, M.; Andrusiv, H.; Bodnarchuk, M. I.; Stöferle, T.; Mahrt, R. F.; Naumenko, D.; Amenitsch, H.; Rainò, G.; Kovalenko, M. V. Monodisperse Long-Chain Sulfobetaine-Capped CsPbBr₃ Nanocrystals and Their Superfluorescent Assemblies. *ACS Cent. Sci.* **2021**, *7*, 135–144.

(73) Willmott, P. R.; Meister, D.; Leake, S. J.; Lange, M.; Bergamaschi, A.; Boge, M.; Calvi, M.; Cancellieri, C.; Casati, N.; Cervellino, A. The Materials Science Beamline Upgrade at the Swiss Light Source. *J. Synchrotron Rad.* **2013**, *20*, 667–682.

NOTE ADDED AFTER ASAP PUBLICATION

Figure 1 was corrected on February 8, 2024.